Circulation
JOURNAL OF THE AMERICAN HEART ASSOCIATION

American Heart Association.
Learn and Live.

Defective Regulation of Interdomain Interactions Within the Ryanodine Receptor Plays a Key Role in the Pathogenesis of Heart Failure

Tetsuro Oda, Masafumi Yano, Takeshi Yamamoto, Takahiro Tokuhisa, Shinichi Okuda, Masahiro Doi, Tomoko Ohkusa, Yasuhiro Ikeda, Shigeki Kobayashi, Noriaki Ikemoto and Masunori Matsuzaki

Circulation 2005;111;3400-3410; originally published online Jun 20, 2005;
DOI: 10.1161/CIRCULATIONAHA.104.507921
Circulation is published by the American Heart Association. 7272 Greenville Avenue, Dallas, TX 72514
 Print ISSN: 0009-7322. Online ISSN: 1524-4539

Defective Regulation of Interdomain Interactions Within the Ryanodine Receptor Plays a Key Role in the Pathogenesis of Heart Failure

Tetsuro Oda, MD*; Masafumi Yano, MD, PhD*; Takeshi Yamamoto, MD, PhD; Takahiro Tokuhisa, MD; Shinichi Okuda, MD, PhD; Masahiro Doi, MD, PhD; Tomoko Ohkusa, MD, PhD; Yasuhiro Ikeda, MD, PhD; Shigeki Kobayashi, MD, PhD; Noriaki Ikemoto, PhD; Masunori Matsuzaki, MD, PhD

Background—According to our hypothesis, 2 domains within the ryanodine receptor (RyR) of sarcoplasmic reticulum (SR) (N-terminal [0 to 600] and central [2000 to 2500] domains), where many mutations have been found in patients with polymorphic ventricular tachycardia, interact with each other as a regulatory switch for channel gating. Here, we investigated whether the defective FKBP12.6-mediated stabilization of RyR in heart failure is produced by an abnormal interdomain interaction.

Methods and Results—SR vesicles were isolated from dog left ventricular muscles, and then the RyR moiety of the SR was fluorescently labeled with methylcoumarin acetate (MCA) using DPc10, a synthetic peptide corresponding to Gly^{2460}-Pro^{2495} of RyR (one of the mutable domains in polymorphic ventricular tachycardia), as a site-directing carrier; the carrier was removed from the RyR after MCA labeling. Addition of DPc10 induced an unzipped state of the interacting N-terminal and central domains, as evidenced by an increase in the accessibility of the RyR-bound MCA fluorescence to a large fluorescence quencher. Domain unzipping resulted in Ca^{2+} leak through the RyR and facilitated cAMP-dependent hyperphosphorylation of RyR and FKBP12.6 dissociation from RyR. When DPc10 was introduced into the isolated myocytes, the magnitude of intracellular Ca^{2+} transient decreased, and its decay time was prolonged. In the SR isolated from pacing-induced dog failing hearts, the domain unzipping has already occurred, together with FKBP12.6 dissociation and Ca^{2+} leak.

Conclusions—The specific domain interaction within the RyR regulates the channel gating property, and the defectiveness in the mode of the interdomain interaction seems to be the initial critical step of the pathogenesis of heart failure. **(*Circulation*. 2005;111:3400-3410.)**

Key Words: calcium ■ heart failure ■ ion channels ■ sarcoplasmic reticulum

A considerable body of accumulated evidence suggests that disturbed calcium homeostasis is a key mechanism for the pathogenesis of human heart failure.[1–3] Our recent

See p 3342

studies with a canine model of pacing-induced heart failure have shown (1) that the Ca^{2+} release function of the ryanodine receptor (RyR) is defective in heart failure,[1] presumably because of a partial loss of FKBP12.6 from RyR[5] and resultant conformational changes in the RyR,[6] and (2) that this defective regulation of the RyR causes an abnormal Ca^{2+} leak.[6] Marx et al,[7] who investigated a causative mechanism of the partial loss of FKBP12.6 from RyR, found that protein kinase A (PKA)–mediated hyper-phosphorylation of RyR causes dissociation of FKBP12.6 from RyR, which in turn increases the sensitivity of the channel to activating Ca^{2+}. β-Adrenergic receptor blockade has been shown to correct the defective interaction of FKBP12.6 with RyR that is triggered by the PKA-mediated hyperphosphorylation of RyR.[8–10] More recently, we found that a new chemical compound JTV519, the 1,4-benzothiazepine derivative, prevented dissociation of FKBP12.6 from RyR2, hence preventing abnormal conformational change in RyR and the subsequent Ca^{2+} leak.[11] Such preventive effects of JTV519 are manifested in an early developmental stage of heart failure, thereby preventing severe heart failure.[11] Wehrens et al[12] also

Received September 22, 2004; revision received February 19, 2005; accepted March 2, 2005.

From the Department of Medical Bioregulation, Division of Cardiovascular Medicine, Yamaguchi University School of Medicine, Yamaguchi, Japan (T.O., M.Y., T.Y., T.T., S.O., M.D., T.O., Y.I., S.K., M.M.), and Boston Biomedical Research Institute, Watertown, and Department of Neurology, Harvard Medical School, Boston (N.I.), Mass.

*Drs Oda and Yano contributed equally to this work.

Correspondence to Masafumi Yano, MD, PhD, Department of Medical Bioregulation, Division of Cardiovascular Medicine, Yamaguchi University School of Medicine, 1-1-1 Minamikogushi, Ube, Yamaguchi, 755-8505, Japan. E-mail yanoma@yamaguchi-u.ac.jp

Circulation **is available at http://www.circulationaha.org** **DOI: 10.1161/CIRCULATIONAHA.104.507921**

demonstrated that JTV519 increased the affinity of FKBP12.6 for RyR2, which stabilized the closed state of RyR2 channels and prevented abnormal Ca^{2+} leak that would otherwise have triggered ventricular arrhythmias.

To date, >20 RyR2 missense mutations have been found to be linked with 2 inherited forms of sudden cardiac death: catecholaminergic polymorphic or familial polymorphic ventricular tachycardia[13,14] and arrhythmogenic right ventricular cardiomyopathy type 2.[15] All RyR2 mutations cluster into 3 regions of the channel that correspond to 3 malignant hyperthermia/central core disease mutation regions (designated as N-terminal domain, central domain, and channel forming domain) of RyR1. In particular, some mutations of RyR2 reported in cardiac disease patients are located in the regions corresponding to the skeletal N-terminal and central domains harboring most of the malignant hyperthermia mutations that cause an increased Ca^{2+} leak. This suggests that RyR2 shares a common domain-mediated channel regulation mechanism with RyR1 and that the increased Ca^{2+} leak of diseased RyR2 channels may be explained by the altered mode of interdomain interactions as described below.

The concept that the interactions between the N-terminal domain and the central domain of RyR1 are involved in Ca^{2+} channel regulation has emerged from the recent domain peptide probe studies of Yamamoto et al[16] and Yamamoto and Ikemoto.[17] According to this concept, in the resting or nonactivated state, the N-terminal and central domains make close contact at several subdomains (domain zipping). The conformational constraints imparted by the zipped configuration of these 2 domains stabilize and maintain the closed state of Ca^{2+} channel. Stimulation via excitation-contraction coupling or pharmacological agents weakens these critical interdomain contacts, resulting in loss of conformational constraints (domain unzipping) and thus lowering of the energy barrier for Ca^{2+} channel opening. Weakening of these interdomain interactions may also occur via mutation or with the use of synthetic domain peptides. For instance, a cardiac domain peptide (DPc10) corresponding to the Gly^{2460}-Pro^{2495} region of the rabbit RyR2 (equivalent to the Gly^{2459}-Pro^{2491} region of the human RyR2) was found to produce significant activation of the RyR2 Ca^{2+} channel, especially at low Ca^{2+} concentrations (0.1 to 0.3 μmol/L).[18] A single Arg-to-Ser mutation made in DPc10, mimicking the Arg^{2474}-to-Ser^{2471} human mutation, abolished all of the effects that would have been produced by DPc10.[18] These data presented strong evidence that synthetic domain peptides corresponding to key subdomains of RyR2 are capable of mimicking diseased conditions of the RyR2 channel by interfering with the interdomain interaction.

Interestingly, the binding region of FKBP12.6 to RyR2, which seems to be in the 2361 to 2496 residues according to Marx et al,[7] is included in the sequence of DPc10 (2460 to 2495). This suggests the possibility that there is a close mechanistic relationship between the PKA-mediated FKBP12.6 dissociation and abnormal domain-domain interactions such as that seen in the DPc10-mediated channel hypersensitization.

In the present study, using the well-characterized domain peptide DPc10 as a probe, we investigated whether FKBP12.6-mediated stabilization of RyR is linked to the interdomain interactions in cardiac muscle.

Methods

Materials

FK506 was provided by Fujisawa Pharmaceutical Co Ltd. JTV519 was kindly provided by Dr Noboru Kaneko (Dokkyo University).

Animal Disease Model

In beagle dogs weighing 10 to 13 kg, we induced heart failure by continuous application of rapid ventricular pacing at 250 bpm using an externally programmable miniature pacemaker (Medtronic Inc) for 28 days, as described elsewhere.[1,6] The care of the animals and the protocols used were in accord with guidelines laid down by the Animal Ethics Committee of Yamaguchi University School of Medicine.

Preparation of Sarcoplasmic Reticulum vesicles

We prepared sarcoplasmic reticulum (SR) vesicles from dog left ventricle (LV), essentially following the method of Kranias et al,[19] with the modifications described elsewhere.[1,6]

Peptides Used and Peptide Synthesis

We used the 2 domain peptides, DP10c and DP10c-mut: DPc10 (DPc2460-2495), 460GFCPDHKAAMVLFLDRVYGIEVQD-FLLHLLEVGFLP2495; DPc10-mut (DPc2460-2495-mut R2474S), 2460GFCPDHKAAMVLFLDSVYGIEVQDFLLHLLEVGFLP2495. Peptides were synthesized on an Applied Biosystems model 431A synthesizer with Fmoc [*N*-(9-fluorenyl)methoxycarbonyl] as the α-amino protecting group, as described previously.[18] The peptides were cleaved and deprotected with 95% trifluoroacetic acid and purified by reversed-phase high-pressure liquid chromatography.

Ca^{2+} Uptake and Leak Assays

Ca^{2+} uptake and the following Ca^{2+} leak assays were done as described previously.[6,8,11] The amount of Ca^{2+} uptake was measured using ^{45}Ca in the presence of 10 μmol/L ruthenium red and 5 mmol/L oxalate as described previously.[20]

Site-Directed Fluorescent Labeling of the RyR

Specific fluorescent labeling of RyR in SR vesicles was performed using the cleavable hetero-bifunctional cross-linking reagent sulfosuccinimidyl 3-{[2-(7-azido-4-methylcoumarin-3-acetamido) ethyl] dithio}propionate from PIERCE, with DPc10 as a site-specific carrier. This method for the site-directed fluorescent labeling of the RyR2 was basically the same as the method used for the DP4-mediated methylcoumarin acetate (MCA)–labeling of RyR1.[17]

To determine the localization of the MCA binding site, fluorescently labeled microsomes (1 mg/mL) were digested with recombinant calpain II (Calbiochem) added at a ratio of 6 U calpain to 1 mg SR protein in a solution containing 150 mmol/L NaCl and 20 mmol/L MOPS (pH 7.2). Digestion was started by adding 3 mmol/L $CaCl_2$. After digestion for 6 minutes at 22 C, the reaction was stopped by adding 3 mmol/L BAPTA.

Fluorescence Quenching of the MCA Fluorescence Attached to the DPc10 Binding Site

The zipped and unzipped states of RyR were evaluated as described previously.[17] The principle of the fluorescence quench assay of domain unzipping is that a large quencher BSA-QSY is inaccessible to the attached MCA in the zipped state, whereas it becomes accessible to the MCA site in the unzipped state. To form the quencher, QSY 7 carboxylic acid was conjugated with BSA by incubating 5 mmol/L QSY 7 carboxylic acid with 0.5 mmol/L BSA in 20 mmol/L HEPES (pH 7.5) for 60 minutes at 22 C in the dark. Unreacted QSY 7 carboxylic acid was removed by Sephadex G50 gel filtration. Fluorescence quenching by both QSY 7 BSA conjugate (a large quencher) and acrylamide (a small quencher) was performed

by measuring steady-state fluorescence of labeled MCA (excitation, 368 nm; emission, 455 nm) in the presence or absence of chemicals. The data were analyzed with the Stern-Volmer equation.

Immunoblot Analysis

We performed immunoblot analyses for FKBP12.6 as described elsewhere.[6,8,11] Using the method by Marx et al,[7] we achieved coimmunoprecipitation of FKBP12.6 from SR using anti-RyR antibody (Oncogene Research Products), followed by immunoblotting with anti-FKBP12 (C-19) antibody (Santa Cruz Biotechnology). Relative phosphorylation level of RyR was determined by immunoblotting with anti-phosphoRyR2 (P2809), which was kindly provided by Dr Andrew R. Marks (Columbia University).

Isolation of Cardiac Myocytes

Cardiac myocytes were isolated from the LV free wall as described previously in detail.[21] In brief, a wedge of LV free wall perfused by a branch of the left circumflex coronary artery was dissected free of the heart and perfused with collagenase-containing buffer. LV myocardium was minced with scissors in fresh collagenase-containing buffer. Then, rod-shaped adult canine cardiomyocytes were prepared by retrograde perfusion of quickly excised hearts with 95%O_2/5%CO_2–bubbled minimal essential medium (Sigma) supplemented with 50 μmol/L Ca^{2+}, 0.5 mg/mL collagenase B, 0.5 mg/mL collagenase D, and 0.02 mg/mL protease type XIV. The Ca^{2+} concentration was then gradually increased to a final concentration of 1 mmol/L by changing the incubation medium (50 μmol/L, 125 μmol/L, 300 μmol/L, and then 1 mmol/L). The isolated canine cardiomyocytes were transferred to laminin-coated glass culture dishes and incubated for 12 hours at 37 C in 5%CO_2/95%O_2 atmosphere.

Cell Shortening and Ca^{2+} Transient Measurement

Measurements of myocyte cell shortening and intracellular Ca^{2+} were performed using fura-2 AM, as described previously.[22] Cells

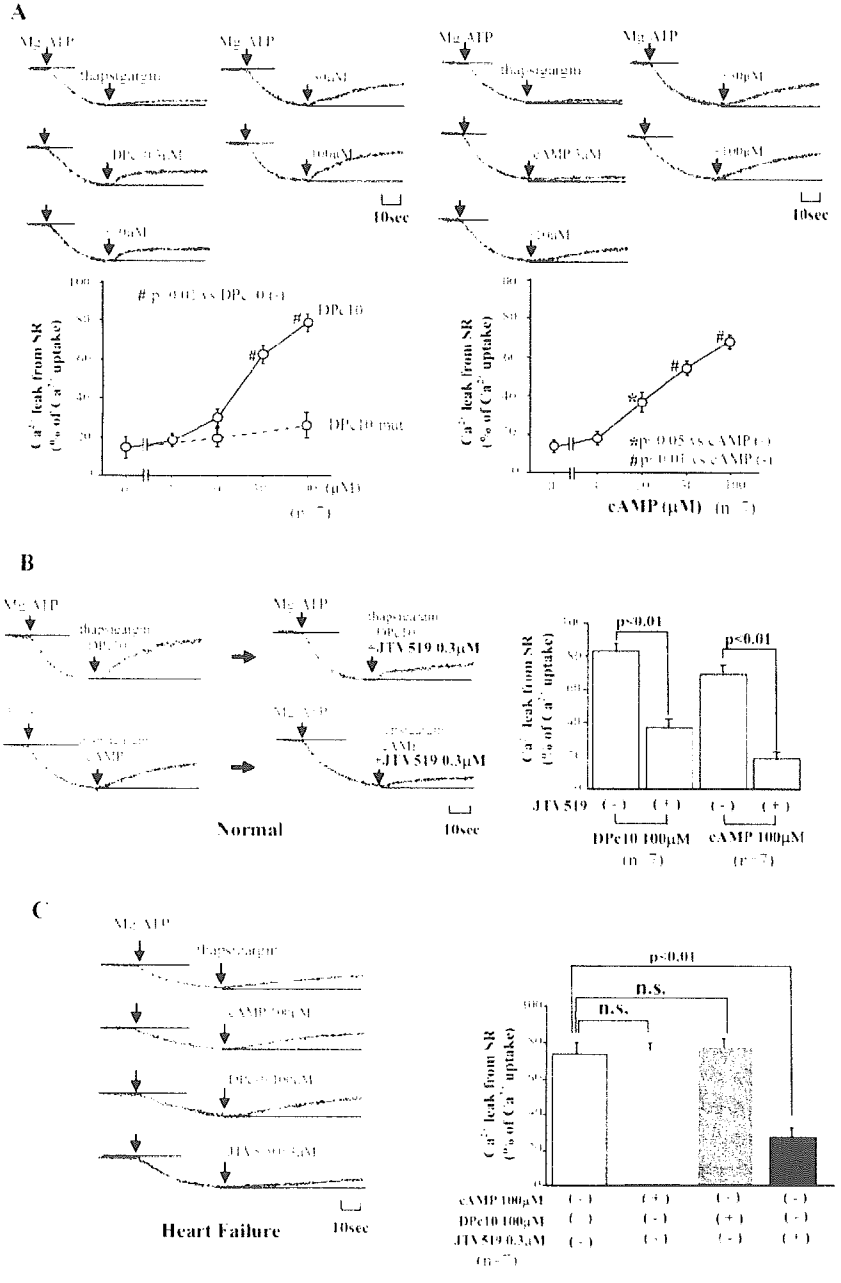

Figure 1. A, Representative time courses of Ca^{2+} uptake and Ca^{2+} leak from SR vesicles in presence of DPc10 or cAMP. B, Effect of JTV519 (0.3 μmol/L) on DPc10-induced or cAMP-induced Ca^{2+} leak. C, Effect of DPc10 or cAMP on spontaneous Ca^{2+} leak in failing SR vesicles.

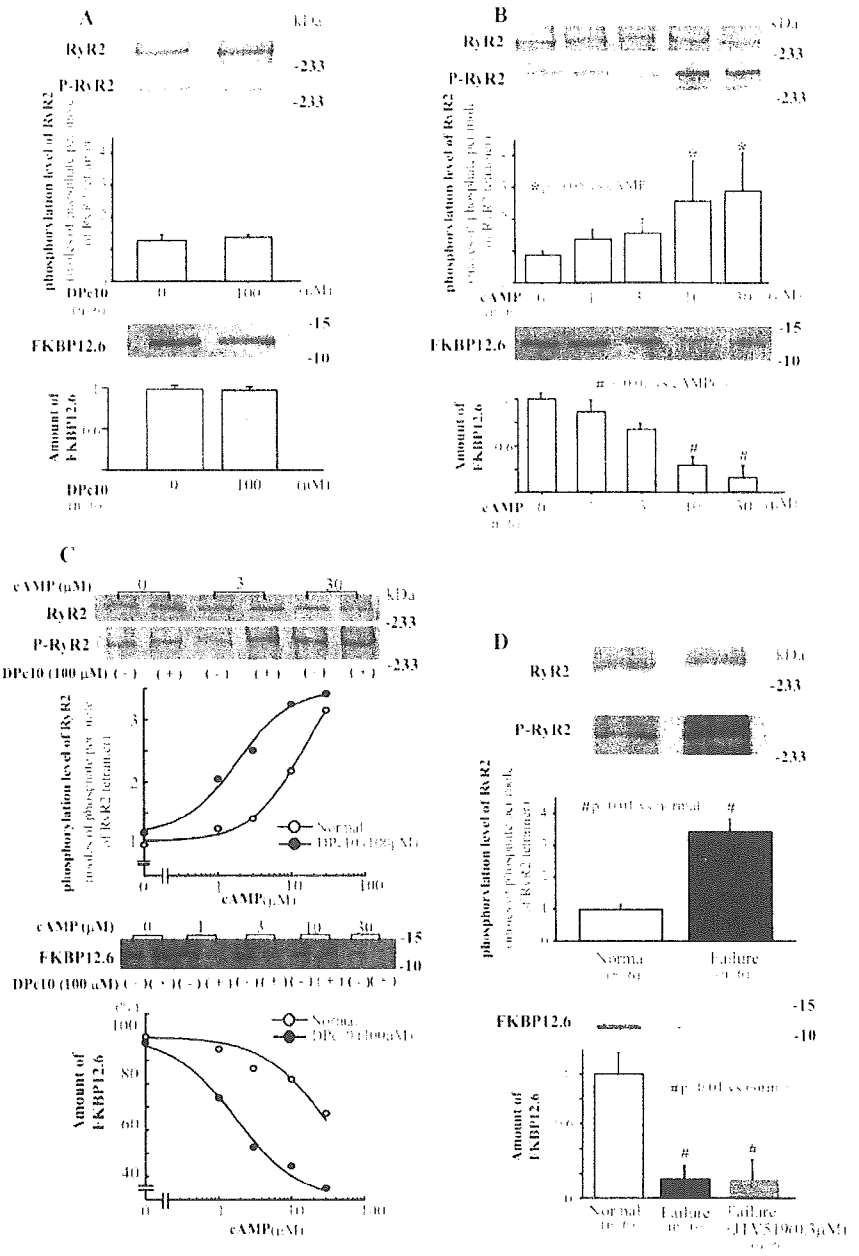

Figure 2. Concentration-dependent effect of DPc10 (A) or cAMP (B) on dissociation of FKBP12.6 from RyR2. Before immunoprecipitation of RyR, SR vesicles were mixed with DPc10 (no cAMP) or cAMP for 30 minutes and then centrifuged, followed by Western blotting. C, Effect of cAMP on PKA phosphorylation level of RyR2 and FKBP12.6 dissociation in presence or absence of DPc10. D, PKA phosphorylation level and amount of FKBP12.6 (with or without 0.3 μmol/L JTV519) in failing SR. Before immunoprecipitation of RyR, SR vesicles were mixed with JTV519 for 30 minutes and then centrifuged, followed by Western blotting.

were stimulated by a field electric stimulator (IonOptix) at a stimulation frequency of 0.5 Hz. After stimulation of the cells, the cell shortening and peak Ca^{2+} transient gradually increased and reached steady state within 1 minute. At the steady state (≈2 minutes after initiation of pacing), the intracellular calcium concentration was monitored by a dual-excitation spectrofluorometer as the ratio of the fluorescence emission intensities (at 505 nm) elicited by excitation at 340 and 380 nm. DPc10 was introduced into the cells with a protein delivery reagent (Bioporter, Gene Therapy Systems, Inc). The successful introduction of DPc10 into the cell was confirmed by detecting the intracellular fluorescence signal of the peptide prelabeled with Alexa Fluor 350 (Molecular Probe). Briefly, DPc10–Alexa Fluor conjugate was formed by incubating 1 mmol/L DPc10 with 1 mmol/L Alexa Fluor carboxylic acid and succinimidyl ester in a 20 mmol/L HEPES buffer (pH 7.6) for 60 minutes at 22 C in the dark. Free Alexa Fluor was removed by Sephadex G15 gel filtration. The final concentration of DPc10 conjugated with the Alexa Fluor was estimated by measuring the absorbance at 280 nm. After the introduction of DPc10-Alexa Fluor conjugate into the cell, the fluorescence intensity of Alexa Fluor was measured with confocal microscopy (LSM 510, Carl Zeiss). The intracellular peptide concentration was determined from the concentration-fluorescence intensity plot.

Statistical Analysis

Statistical analysis was performed by ANOVA with a post hoc Scheffé's test. Data are expressed as mean±SD. We accepted a value of $P<0.05$ as statistically significant.

Results

DPc10 Induces Ca^{2+} Leak and Facilitates PKA-Mediated Hyperphosphorylation and FKBP12.6 Dissociation

Addition of 1 μmol/L thapsigargin to normal SR vesicles at the steady state of ATP-dependent Ca^{2+} uptake produced little Ca^{2+} leak, whereas addition of 10 to 100 μmol/L DPc10,

together with 1 μmol/L thapsigargin, produced a pronounced leak. However, DPc10-mut (10 to 100 μmol/L) did not induce Ca^{2+} leak (Figure 1A). Following ATP-dependent Ca^{2+} uptake after preincubation of the SR vesicles with 3 to 30 μmol/L cAMP plus 1 μmol/L okadaic acid, 1 μmol/L thapsigargin was added. Under the conditions, a pronounced leak was observed (Figure 1A). Both DPc10- and cAMP-induced Ca^{2+} leaks were almost completely inhibited by 0.3 μmol/L JTV519 (Figure 1B). Figure 1C shows the effect of DPc10 and cAMP on the spontaneous Ca^{2+} leak in failing SR. In agreement with our previous reports,[6,8,11] there was a prominent Ca^{2+} leak in the failing SR even in the absence of cAMP or DPc10. Therefore, both cAMP and DPc10 had no further effect on the Ca^{2+} leak. JTV519 (0.3 μmol/L) abolished the spontaneous Ca^{2+} leak that otherwise had been seen in the failing SR. On the other hand, there was no appreciable effect of DPc10 on SR Ca^{2+} uptake (with DPc10, 8.96±3.48 nmol · mg $^{-1}$ · min $^{-1}$; without DPc10, 8.73±1.71 nmol · mg $^{-1}$ · min $^{-1}$; P=0.77).

Figure 2A through 2C shows the concentration-dependent effects of DPc10 or cAMP on the level of phosphorylation of RyR2 and the extent of dissociation of FKBP12.6 from RyR2 in normal SR. In the absence of cAMP, DPc10 had no appreciable effect both on dissociation of FKBP12.6 from RyR2 and on the PKA phosphorylation level (Figure 2A). However, preincubation of the SR vesicles with cAMP for 30 minutes, as in Ca^{2+} leak experiment, led to a dissociation of FKBP12.6 in a concentration-dependent manner concurrently with an increase in the PKA phosphorylation level (Figure 2B).

As shown in Figure 2C, in the presence of 100 μmol/L DPc10, FKBP12.6 dissociation from RyR occurred at a lower concentration of cAMP than in its absence, in parallel with an increase in the PKA phosphorylation level of RyR. This suggests that domain unzipping induces a conformational change that facilitates PKA phosphorylation and FKBP12.6 dissociation. In further support of our previous reports,[6,8,11] the amount of RyR2-bound FKBP12.6 was lower in failing SR than in normal SR, which was inversely proportional to the level of hyperphosphorylation of RyR2 (Figure 2D). The amount of FKBP12.6 was unchanged even in the presence of JTV519, suggesting that the inhibition of Ca^{2+} leak by JTV519 (Figure 1C) is not mediated by rebinding of (RyR-unbound) FKBP12.6 to SR vesicles.

Spectroscopic Monitoring of DPc10- and cAMP-Induced Changes in the Mode of Interdomain Interactions

According to the domain-mediated channel regulation hypothesis (see the Introduction), the above findings suggest that DPc10 produced unzipping of the interacting N-terminal and central domains, which then caused Ca^{2+} leak. To investigate this possibility, we adopted the fluorescence quench technique. The method involves (1) incorporation of the fluorescent probe MCA into a key site of the interacting N-terminal and central domain pair in a site-specific manner by using DPc10 as a site-direction carrier, (2) localization of the site of MCA attachment within the polypeptide chain of RyR2, and (3) examination of the accessibility of the incorporated MCA probe to a large fluorescence quencher. Figure

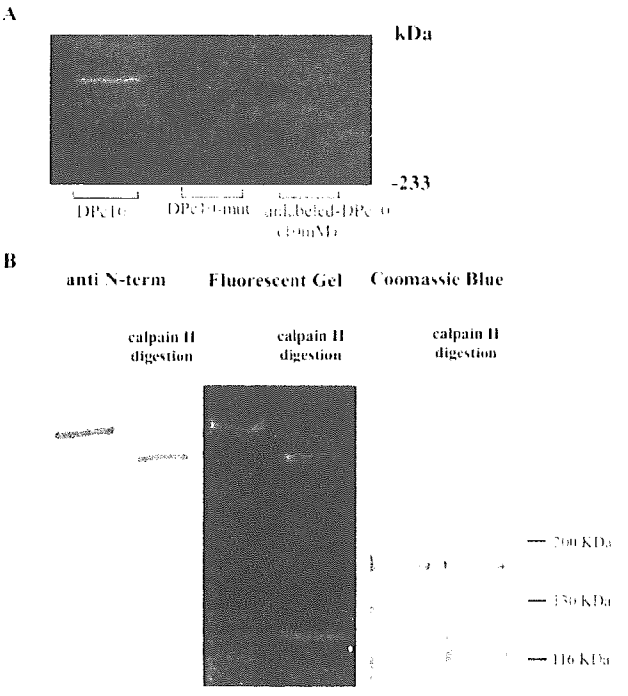

Figure 3. A, Site-directed fluorescence labeling of RyR2 with MCA. MCA fluorescence labeling took place only when DPc10 was used to mediate site-specific labeling (left lane). No MCA fluorescence was seen when DPc10-mut was used (middle lane) or when an excess concentration of DPc10 (10 mmol/L) was added during the labeling (cold chase, right lane). B, Localization of MCA binding site after digestion with calpain II. Fluorescently labeled microsomes (1 mg/mL) were digested with recombinant calpain II added at ratio of 6 U calpain to 1 mg SR protein. Note that site of MCA labeling is localized in exactly same fragments as stained by anti–N-terminal antibody. Anti–N-terminal antibody (rabbit serum) was raised against peptide ^{24}CTATIHKEQQKL^{35}.

3A shows that the carrier DPc10 mediated an intense fluorescence labeling of the RyR2 band (left lane), but DPc10-mut could not mediate MCA labeling (middle lane). As shown in the "cold-chase" experiment shown in the right lane, an excess concentration of unlabeled DPc10 (10 mmol/L) prevented DPc10-mediated MCA labeling. Figure 3B shows the results of our attempt to localize the site of MCA attachment within the RyR2 polypeptide chain. As shown in the Coomassie blue–stained gels, digestion of the SR with calpain II (6 U/mg protein) cleaved the RyR2 into several fragments. Of these fragments, 2 fragments, a 410-kDa fragment and a 120-kDa fragment, retain the MCA label (fluorescent gel). Importantly, polyclonal antibody raised against the peptide corresponding to the ^{24}CTATIHKEQQKL^{35} region of RyR2 reacted specifically with the MCA-labeled 410- and 120-kDa fragments (anti N-term). These results suggest that DPc10-mediated specific MCA labeling has taken place in the 120-kDa N-terminal region of RyR2. That the peptide corresponding to the central domain region has introduced the MCA label to the N-terminal region supports the idea that there is a close interaction between the N-terminal domain and the central domain, as predicted from the hypothesis (see the Introduction).

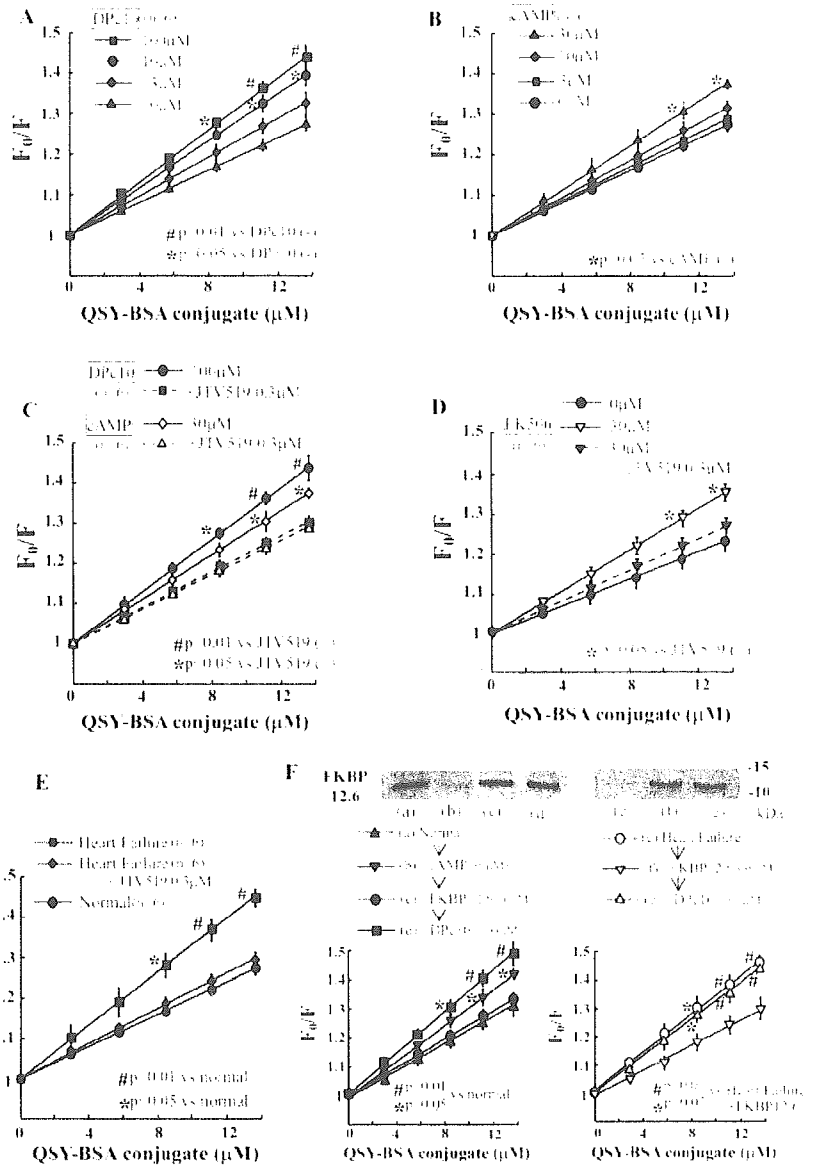

Figure 4. Stern-Volmer plots of fluorescence quenching data with QSY-BSA in absence and presence of DPc10 (A) or cAMP (B) in normal SR. In presence of DPc10 or cAMP, accessibility of bound MCA to quencher (slope of plot) became significantly larger than that in its absence. Effect of JTV519 on Stern-Volmer plots of fluorescence quenching by QSY-BSA in normal (C, D) and failing (E) SR. JTV519 reversed increased accessibility of MCA to quencher that has been produced by DPc10, cAMP (C), and FK506 (D). FK506 was used to dissociate FKBP12.6 from RyR in normal SR (D). Note that accessibility of MCA to quencher (ie, degree of domain unzipping) in failing SR is larger than that of normal SR, but in presence of JTV519, former became about same as latter (E). Effect of FKBP12.6 reconstitution into FKBP12.6-depleted RyR2 on accessibility of bound MCA to quencher (F). Normal SR vesicles were mixed with 30 μmol/L cAMP for 30 minutes and then centrifuged, followed by addition of 30 nmol/L recombinant FKBP12.6, together with alkaline phosphatase for dephosphorylation of RyR2 (1:100 enzyme to protein),[7] in presence or absence of 100 μmol/L DPc10. Same procedure, except for addition of cAMP, was performed also in failing SR vesicles. Note that FKBP12.6 rebinding restored zipped state that could be unzipped again in both cAMP-treated normal and failing SR vesicles.

The MCA probe attached to the critical domain would be inaccessible to a bulky fluorescence quencher (QSY-BSA conjugate) in the zipped configuration, but it would become accessible to the quencher on unzipping (see Methods). To monitor the zipped and unzipped states of RyR2, we used QSY-BSA as a large quencher (Figure 4). Similar to the case of the recent report with DP4,[17] the slope of the Stern-Volmer plot (K_Q), which represents the accessibility to the quencher, namely the degree of domain unzipping, was considerably increased by DPc10, indicating that DPc10 induced domain unzipping (Figure 4A). However, when we used, acrylamide, the small quencher, DP10 had virtually no effect on the efficiency of the MCA fluorescence quenching (not shown). These results suggest that the domain unzipping may involve a sizable opening of the gap between the interacting domains. Like DPc10, 30 μmol/L cAMP increased the K_Q, although the extent of the increase was about half of the DPc10 (100 μmol/L)–induced increase (Figure 4B). Collectively, DPc10 induces domain unzipping; however, domain unzipping does not induce FKBP dissociation by itself. Rather, it seems to facilitate FKBP dissociation in response to PKA-mediated hyperphosphorylation of RyR.

As shown in Figure 4C, both DPc10- and cAMP-induced increases in the extent of fluorescence quenching were almost completely reversed by JTV519. Addition of FK506 that dissociates FKBP12.6 from RyR also increased the K_Q, and again, JTV519 reversed it (Figure 4D). This is particularly important in view of our previous finding[11] that in the presence of JTV519, FK506-induced FKBP12.6 dissociation from RyR2 was partially inhibited and reassociation of FKBP12.6 to RyR2 was enhanced in failing SR (Figure 3 in Reference 11). Taken together, these results suggest that JTV519 stabilizes the zipped configuration of the interacting domains and thus prevents FKBP12.6 dissociation and Ca^{2+} leak.

Interestingly, the extent of fluorescence quenching (K_Q) in failing heart SR without the addition of domain-unzipping reagents (DPc10 or cAMP) was about the same as that in the

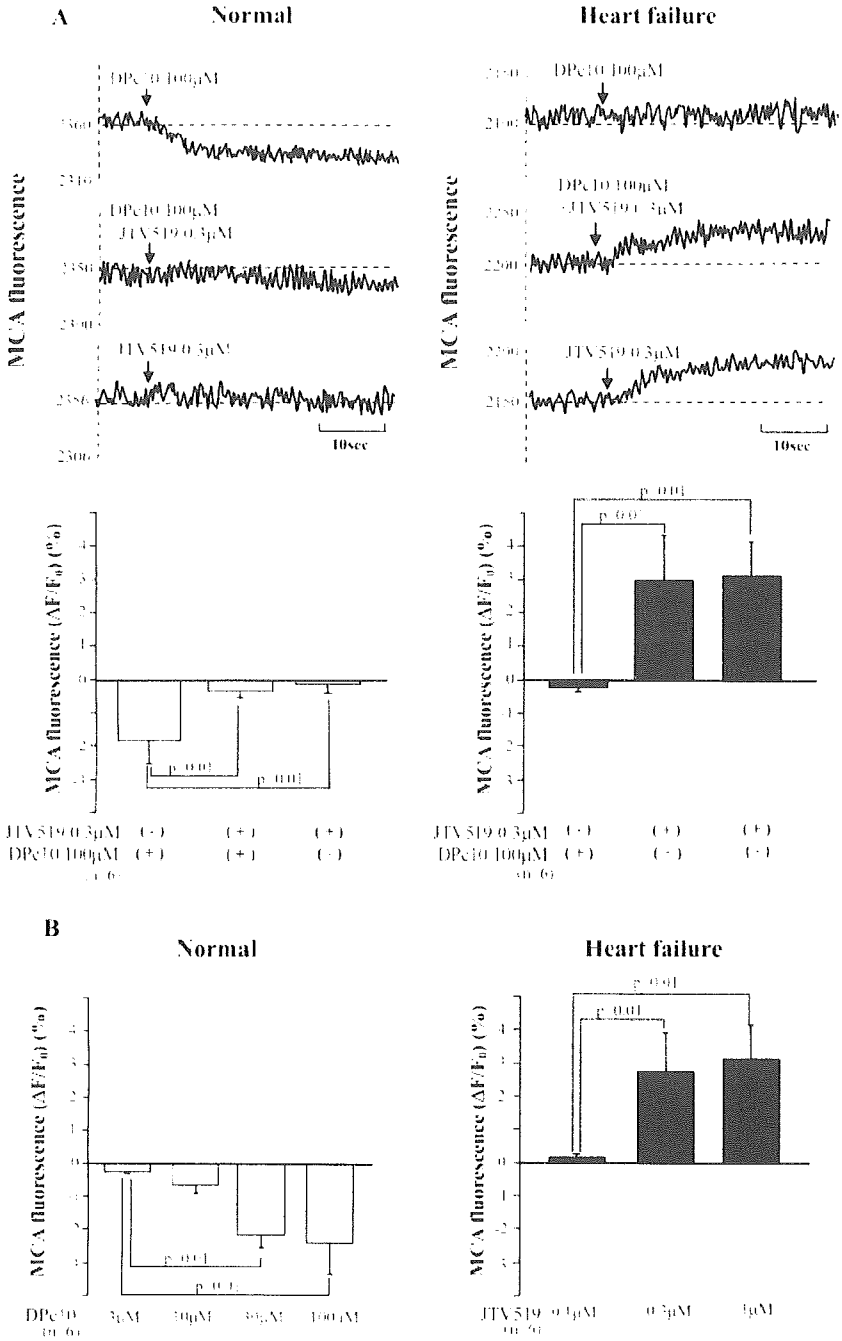

Figure 5. A, Effects of DPc10 and JTV519 on representative time courses of changes in MCA fluorescence during Ca^{2+} leak in SR vesicles isolated from normal and failing (4w-pacing) dog hearts. Changes in MCA fluorescence (in percent control) were calculated as $(F-F_0)/F_0 \cdot 100$ (%), where F_0 is fluorescence intensity before addition of DPc10 or JTV519 (baseline) and F is fluorescence intensity after addition of DPc10 or JTV519. B, Concentration-dependent effects of DPc10 or JTV519 on changes in MCA fluorescence in normal and failing SR vesicles.

normal SR that had been treated with DPc10 (Figure 4E). However, JTV519 reduced the K_Q to a normal level in failing SR. These findings suggest that domain unzipping had already occurred in failing SR, causing Ca^{2+} leak and FKBP dissociation, and that JTV519 restored the zipped state and then restored normal channel function and a normal state of FKBP association. To further elucidate whether domain unzipping can be reversed by FKBP12.6 rebinding, we performed an FKBP12.6 reconstitution experiment under dephosphorylation conditions of RyR2 using alkaline phosphatase.[7] As shown in Figure 4F, phosphatase treatment and FKBP12.6 rebinding restored a zipped state that could again be unzipped by DPc10 in both cAMP-treated normal SR and failing SR. In the presence of phosphatase, the amount of the re-bound FK12.6 was about the same among the normal SR, cAMP-treated normal SR, and failing SR, presumably because the phosphatase inhibits phosphorylation of RyR2 and hence restores the FKBP12.6 rebinding.

To further characterize local conformation in the vicinity of the DPc10-mediated MCA attachment site in normal and diseased conditions, we investigated the effects of DPc10 or JTV519 on the fluorescence intensity of the attached MCA. As shown in Figure 5A, DPc10 induced a rapid decrease in the fluorescence signal in normal SR, which was inhibited by

In Vivo Cell Shortening and Ca^{2+} Transient in Normal and Failing Myocytes

	Cell Shortening, %			Peak High, %			Time From Peak to 70% Decline, ms		
	(−)	Iso 50 nmol/L	FSK 500 nmol/L	(−)	Iso 50 nmol/L	FSK 500 nmol/L	(−)	Iso 50 nmol/L	FSK 500 nmol/L
Untreated (n=30)	8.9±1.8	...	...	33.0±9.7	...	...	88.0±21.0	...	...
DPc10-mut(+) Bioporter(+)	9.0±2.2	...	...	32.0±11.7	...	...	91.3±16.4	...	...
DPc10-mut(−) Bioporter(+)	8.8±2.1	...	...	31.9±13.4	...	...	92.0±10.0	...	...
Normal (n=100)									
Untreated	9.0±2.2	14.5±3.2‖	12.4±1.8‖	32.0±11.7	65.5±17.8‖	52.4±7.4‖	91.3±16.4	55.5±9.5‖	63.6±9.0‖
DPc10(+) JTV519(−)	2.4±0.6*	4.4±1.2†	3.2±1.2†	13.6±4.8*	17.1±5.3†	15.2±6.0†	108.3±36.4*	98.5±28.6*	106.1±30.3*
DPc10(+) JTV519(+)	6.2±2.4‡	12.1±1.4§‖	11.5±2.3§‖	24.0±6.5‡	47.6±13.5§‖	43.9±8.5§‖	94.6±8.5#	63.4±17.6‡‖	67.2±9.9‡‖
Heart failure (n=100)									
JTV519(−)	1.9±0.6	2.1±0.7	2.0±0.3	14.4±4.6	20.1±1.7	17.1±4.2	112.2±31.5	92.3±17.4	105.0±17.2
JTV519(+)	5.7±0.9§	10.1±3.1§‖	9.4±2.6§‖	28.6±4.6‡	42.6±13.1‡‖	40.7±11.0‡‖	98.2±10.3	62.9±26.2‡‖	61.9±20.6‡‖

Iso indicates isoproterenol; FSK, forskolin.

*$P<0.05$, †$P<0.01$, untreated vs DPc10(+) and JTV519(−); ‡$P<0.05$, §$P<0.01$, DPc10(+) and JTV519(−) vs DPc10(+) and JTV519(+) in normal myocytes, or JTV519(−) vs JTV519(+) in failing myocytes; ‖$P<0.05$ vs Iso(−) and FSK(−).

JTV519. The fluorescence intensity of the attached MCA is expected to decrease when the environment of the MCA site changes from hydrophobic to hydrophilic on domain unzipping. Thus, these results provide further evidence that DPc10 produced domain unzipping and JTV519 reversed it. In failing SR, DPc10 produced virtually no effect on the MCA fluorescence, presumably because domain unzipping had already taken place. On addition of JTV519, however, the MCA fluorescence increased to a higher level, indicating restored zipped state. Figure 5B shows the concentration-dependent effects of DPc10 or JTV519 on the changes in MCA fluorescence in normal and failing SR vesicles. DPc10 decreased the level of MCA fluorescence in a concentration-dependent manner in normal SR (reflecting the change from the zipped to the unzipped state), whereas JTV519 increased the MCA fluorescence level in failing SR (reflecting the restoration of the zipped state).

Effects of DPc10 on Ca^{2+} Transients and Cell Shortening

To investigate the effect of DPc10-induced domain unzipping in in vivo conditions, we introduced DPc10 into the cardiac myocytes and investigated both Ca^{2+} transient and cell shortening simultaneously (the Table and Figure 6). To evaluate the efficiency of DPc10 introduction into the cell by the protein delivery regent, Alexa Fluor 350–DPc10 conjugate was mixed with the protein delivery reagent. The Alexa Fluor fluorescence signal was clearly observed in all myocytes, indicating successful DPc10 introduction into myocytes by this method (Figure 6A). There was no statistically significant difference in the estimated concentration of DPc10 (see Methods) between JTV-treated (2.92±0.65 μmol/L) and untreated DPc10-introduced myocytes (2.91±0.71 μmol/L; $P=0.82$). As shown in Figure 6B, neither protein delivery reagent (Bioporter) alone nor DPc10-mut (R2474S) with Bioporter had any significant effect on cell shortening and Ca^{2+} transient. This suggests that protein delivery reagent has no direct effect on myocyte function and that DPc10-mut does not interact with RyR and has no effect on myocyte functions. As shown in Figure 6C, in response to isoproterenol or forskolin, the duration of Ca^{2+} transient was shortened and its peak was increased in the untreated myocyte. In the DPc10-introduced myocytes, the duration of Ca^{2+} transient was prolonged, its peak was decreased, and the diastolic level of cytoplasmic $[Ca^{2+}]$ was increased. However, isoproterenol or forskolin produced no significant change in the Ca^{2+} transient in these myocytes. Because DPc10 did not change SR Ca^{2+} uptake function, as mentioned earlier, these results suggest that, as in the aforementioned in vitro experiments, DPc10 produced domain unzipping and then Ca^{2+} leak. The increase in cell shortening in response to isoproterenol or forskolin was less in the DPc10-treated myocyte than the untreated myocyte (Table). Coincubation with JTV519 (0.3 μmol/L) restored normal activities of both Ca^{2+} transient and cell shortening in the DPc10-treated myocyte. These findings, consistent in both in vitro and in vivo studies, suggest that the conformational state of the interacting domains (zipped or unzipped) is a critical factor for tuning the channel gating and for Ca^{2+} homeostasis in normal and diseased myocytes.

As shown in Figure 6D, Ca^{2+} transient and cell shortening in the myocytes isolated from the pacing-induced failing dog hearts were deteriorated compared with those in normal myocytes. The diastolic level of the cytoplasmic $[Ca^{2+}]$ was higher in failing myocytes than in normal myocytes. In response to isoproterenol or forskolin, both Ca^{2+} transient and cell shortening were partially restored toward normal by JTV519 (0.3 μmol/L). There was no significant difference in the Ca^{2+} transient and cell shortening properties between DPc10-treated and untreated failing myocytes (data not shown).

Because intracellular peak Ca^{2+} transient strongly depends on the SR Ca^{2+} loading, we hypothesized that SR Ca^{2+} loading may be reduced as a result of Ca^{2+} leak in DPc10-

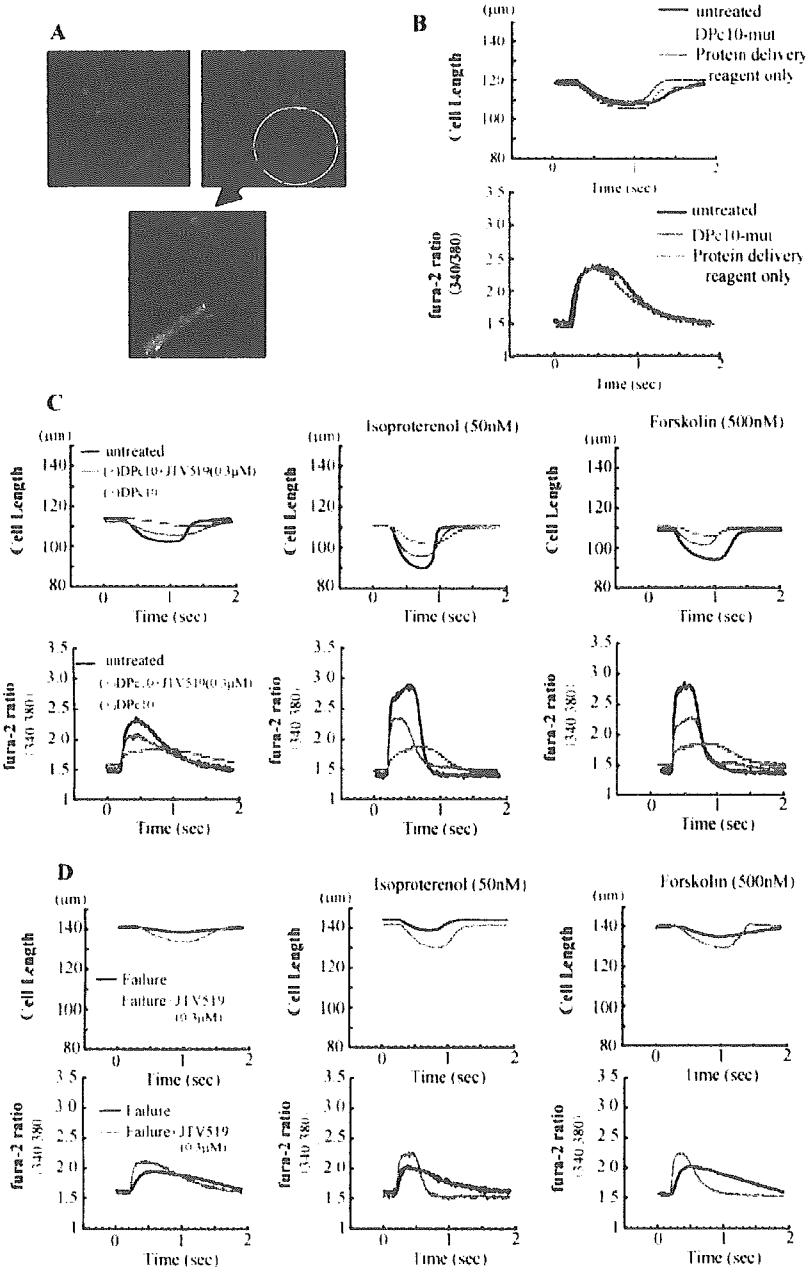

Figure 6. A, Delivery of DPc10 fluorescently labeled with Alexa Fluor 350 into isolated myocytes. Confocal microscopy clearly detects fluorescence signal of DPc10 in myocytes. Cell surface membrane was fluorescently labeled as red by wheat germ agglutinin–Alexa Fluor 633 conjugate. B, Cell shortening and Ca^{2+} transient in presence of either DPc10-mut or protein delivery reagent only compared with untreated normal myocyte. C, Ca^{2+} transient and cell shortening in DPc10-untreated and DPc10-treated normal myocytes in presence or absence of various effectors: JTV519, isoproterenol, and forskolin. D, Ca^{2+} transient and cell shortening in failing myocytes in presence or the absence of various effectors: JTV519, isoproterenol, and forskolin.

introduced myocytes and that it may be increased with JTV519 by preventing the Ca^{2+} leak. To test this hypothesis, we performed caffeine application experiments (Figure 7). In DPc10-introduced normal myocytes, peak Ca^{2+} transient after addition of caffeine was reduced, whereas it was restored toward normal in the presence of JTV519 (Figure 7, top). In failing myocytes in which the peak Ca^{2+} transient after addition of caffeine was lower than in normal myocytes, JTV519 increased it (Figure 7, bottom). These findings suggest that prevention of Ca^{2+} leak by JTV519 is effective in increasing myocyte contractility by increasing SR Ca^{2+} loading.

Discussion

The most important finding deduced from this study is that the defective interdomain interaction may play a key role in abnormal Ca^{2+} leak and subsequent contractile and relaxation dysfunctions seen in heart failure. This conclusion is based on the following findings. First, DPc10 (10 to 100 μmol/L) induced domain unzipping (Figure 4A) and the subsequent Ca^{2+} leak (Figure 2A). DPc10-induced domain unzipping did not induce FKBP12.6 dissociation by itself, but it facilitated FKBP dissociation in response to PKA-mediated hyperphosphorylation (Figure 2C). Alternately, FKBP dissociation either by PKA phosphorylation or FK506 induced domain unzipping (Figure 4B) and Ca^{2+} leak (Figure 2B). This domain unzipping was reversed by JTV519 (Figure 4C and 4D). Thus, domain unzipping and FKBP dissociation produce synergistic effects via conformational changes in the vicinity of interacting domains, and JTV519 may prevent the conformational change. Second, in failing hearts, the unzipped state

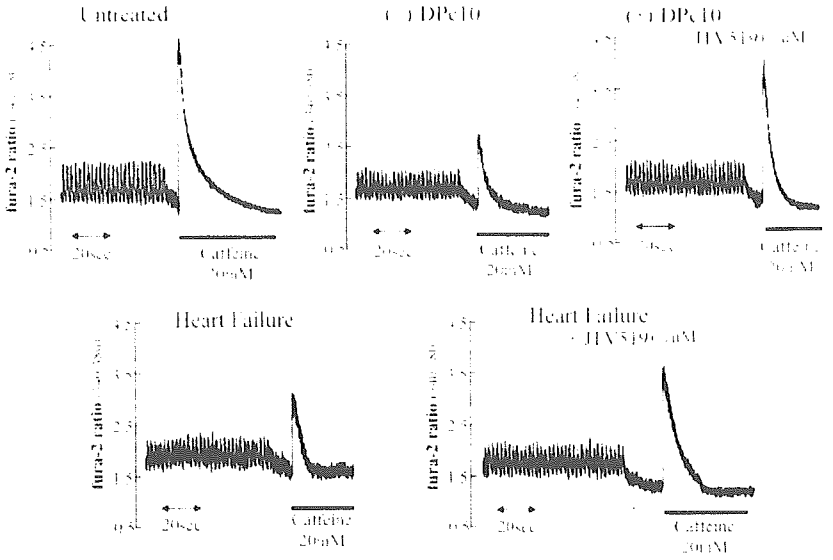

Figure 7. Representative time courses of Ca^{2+} transients before and after addition of caffeine in normal and failing myocytes. Caffeine-induced increase in Ca^{2+} transients reflecting SR Ca^{2+} load was measured after stimulation train at 0.5 Hz by rapidly switching superfusing solution to one containing 20 mmol/L caffeine for 5 to 6 seconds. Note that peak Ca^{2+} transient after addition of caffeine (measure of SR Ca^{2+} load) was higher in normal myocytes than in failing myocytes and that JTV treatment (0.3 μmol/L) ameliorated SR load by inhibiting SR Ca^{2+} leak.

has already taken place, but JTV519 restored the zipped state (Figure 4E). Thus, JTV519 stopped Ca^{2+} leak completely (Figure 1C), even though much of the FKBP12.6 had already been dissociated from RyR by hyperphosphorylation of RyR (Figure 2D). Third, in the experiment with isolated myocytes, the DPc10-introduced myocytes showed a prolonged duration of Ca^{2+} transient and a decreased velocity in cell shortening (Figure 6C). These abnormalities were corrected by the addition of JTV519 (Figure 6C). The SR Ca^{2+} content, assessed by rapid application of caffeine, was reduced both in DPc10-introduced normal myocytes and in failing myocytes, but it was restored by JTV519. This suggests that the inhibition of SR Ca^{2+} leak by JTV519 increased SR Ca^{2+} content and thereby augmented cell shortening (Figure 7). Thus, both in vitro and in vivo experiments carried out in the present study consistently support the notion that the unzipped state of the interacting domains plays a key role in various episodes seen in failing heart such as FKBP dissociation, hyperphosphorylation, and SR Ca^{2+} leak. This notion is further supported by the fact that phosphatase treatment and FKBP12.6 rebinding restore the zipped state that can be unzipped again by DPc10. Thus, it seems that restoration of the domain interaction from the unzipped to the zipped states is a new strategy for the treatment of polymorphic ventricular tachycardia and posttranslationally developed heart failure as well. Reduction of the Ca^{2+} leak seems to be advantageous from an energy point of view because SR Ca^{2+} leak itself requires increased SERCA2a activity to maintain a physiological level of cytosolic Ca^{2+}.

It was shown that mutations in RyR2 (S2246L, R2474S, R4497C) linked to exercise-induced arrhythmias (in patients with catecholaminergic polymorphic ventricular tachycardia) reduced the affinity of FKBP12.6 for RyR2 and increased single-channel activity after PKA phosphorylation.[23] It should be noted that one of these mutations, R2474S, is the same mutation we have made in DPc10-mut. The present finding that DPc10 produced diseaselike effects but DPc10-mut did not is consistent with our prediction that DPc10, but not DPc10-mut, is capable of interfering with the domain-domain interaction and producing a domain unzipping effect (see hypothesis in the Introduction). These results present valuable evidence that synthetic domain peptide was capable of mimicking native conformation of the corresponding in vivo domain, and the data obtained with the peptide are physiologically relevant. Indeed, the fact that DPc10 increased the sensitivity of PKA phosphorylation–induced FKBP12.6 dissociation to cAMP in the SR (Figure 2C) is consistent with the recent finding that catecholaminergic polymorphic ventricular tachycardia–linked mutant RyR2 channels have a decreased affinity for FKBP12.6 and display abnormal single-channel function after PKA phosphorylation.[23]

Although RyR2 has been shown to be hyperphosphorylated, correlating with FKBP12.6 dissociation both in various experimental models of heart failure[6,7,24] and in human heart failure,[7,10] the functional role of RyR phosphorylation by PKA remains to be elucidated. Li et al[25] found that PKA phosphorylation of RyR did not increase calcium sparks in permeabilized myocytes when the cytosolic Ca^{2+} was clamped at 50 or 10 nmol/L, lower than diastolic Ca^{2+} concentrations. They also recently showed that PKA phosphorylation induced by isoproterenol significantly increased the rate of Ca^{2+} release without changing the amplitude of Ca^{2+} release when both SR Ca^{2+} load and Ca^{2+} current were held constant.[26] This suggests that a major outcome of PKA-dependent phosphorylation of RyR2 is an increase in the excitation-contraction coupling gain during exercise and stress.

The data shown in this study suggest that abnormal RyR2 channel functions in failing hearts are caused by 3 major factors: domain unzipping, an increased level of PKA phosphorylation, and dissociation of the receptor-bound FKBP12.6. As shown here, domain unzipping facilitated PKA phosphorylation and the resultant FKBP12.6 dissociation (Figure 2C) in normal SR. In the absence of cAMP, DPc10 caused domain unzipping and Ca^{2+} leak, without causing any changes in the level of phosphorylation and in the amount of the RyR2-bound FKBP12.6. These results

suggest that the increased tendency of domain unzipping may be the primary cause of the increased Ca^{2+} leak. However, the present data also show that the increased phosphorylation and FKBP12.6 dissociation produce SR Ca^{2+} leak directly or by facilitating domain unzipping. Thus, a reasonable conclusion of the present study seems to be that these 3 factors—domain unzipping, hyperphosphorylation, and FKBP12.6 dissociation—produce synergetic effects on Ca^{2+} leak in a cooperative manner.

As shown here, JTV519 inhibits DPc10-induced domain unzipping and prevents Ca^{2+} leak, and again, in the absence of cAMP, JTV519 has no effect on phosphorylation and the receptor-bound FKBP12.6 (data not shown). This suggests that the mechanism of pharmacological action of JTV519 is to stabilize the interdomain interaction and in turn to prevent FKBP12.6 dissociation and Ca^{2+} leak. In further support of this notion, we found that the amount of the RyR2-bound FKBP12.6 in failing heart remained identical in the absence or presence of JTV519. However, we cannot analyze the possibility that the improvement in myocyte function by JTV519 in failing myocyte (Figure 6D and the Table) might be caused by rebinding of the once-dissociated FKBP12.6 to RyR2; no method is available at the moment that permits us to determine the amount of RyR2-bound FKBP12.6 in situ.

In conclusion, defective interactions of the regulatory domains in RyR2 seem to play a key role in the abnormal Ca^{2+} channel functions of RyR2 seen in the SR of failing hearts such as increased Ca^{2+} leak and dissociation of FKBP12.6. The present finding that the defective domain interaction is corrected by JTV519 provides one with a new clue for the development of therapeutic strategy against heart failure and possibly cardiac arrhythmia.

Acknowledgments

This work was supported by grants-in-aid for scientific research from the Ministry of Education in Japan (grants 16590689, 16209026, and 14370228 to Drs Yano and Matsuzaki), by the Takeda Science Foundation (to Dr Yano), and by National Institutes of Health grant HL-072841 (to Dr Ikemoto).

References

1. Marks AR. Ryanodine receptors/calcium release channels in heart failure and sudden cardiac death. *J Mol Cell Cardiol*. 2001;33:615–624. Review.
2. Hasenfuss G. Alterations of calcium-regulatory proteins in heart failure. *Cardiovasc Res*. 1998;37:279–289. Review.
3. Marks AR. Cardiac intracellular calcium release channels: role in heart failure. *Circ Res*. 2000;87:8–11.
4. Yamamoto T, Yano M, Kohno M, Hisaoka T, Ono K, Tanigawa T, Saiki Y, Hisamatsu Y, Ohkusa T, Matsuzaki M. Abnormal Ca^{2+} release from cardiac sarcoplasmic reticulum in tachycardia-induced heart failure. *Cardiovasc Res*. 1999;44:146–155.
5. Ono K, Yano M, Ohkusa T, Kohno M, Hisaoka T, Tanigawa T, Kobayashi S, Kohno M, Matsuzaki M. Altered interaction of FKBP12.6 with ryanodine receptor as a cause of abnormal Ca^{2+} release in heart failure. *Cardiovasc Res*. 2000;48:323–331.
6. Yano M, Ono K, Ohkusa T, Suetsugu M, Kohno M, Hisaoka T, Kobayashi S, Hisamatsu Y, Yamamoto T, Kohno M, Noguchi N, Takasawa S, Okamoto H, Matsuzaki M. Altered stoichiometry of FKBP12.6 versus ryanodine receptor as a cause of abnormal Ca^{2+} leak through ryanodine receptor in heart failure. *Circulation*. 2000;102:2131–2136.
7. Marx SO, Reiken S, Hisamatsu Y, Jayaraman T, Burkhoff D, Rosemblit N, Marks AR. PKA phosphorylation dissociates FKBP12.6 from the calcium release channel (ryanodine receptor): defective regulation in failing hearts. *Cell*. 2000;101:365–376.
8. Doi M, Yano M, Kobayashi S, Kohno M, Tokuhisa T, Okuda S, Suetsugu M, Hisamatsu Y, Ohkusa T, Kohno M, Matsuzaki M. Propranolol prevents the development of heart failure by restoring FKBP12.6-mediated stabilization of ryanodine receptor. *Circulation*. 2002;105:1374–1379.
9. Reiken S, Gaburjakova M, Gaburjakova J, He KL, Prieto A, Becker E, Yi GH, Wang J, Burkhoff D, Marks AR. β-Adrenergic receptor blockers restore cardiac calcium release channel (ryanodine receptor) structure and function in heart failure. *Circulation*. 2001;104:2843–2848.
10. Reiken S, Wehrens XH, Vest JA, Barbone A, Klotz S, Mancini D, Burkhoff D, Marks AR. β-Blockers restore calcium release channel function and improve cardiac muscle performance in human heart failure. *Circulation*. 2003;107:2459–2466.
11. Yano M, Kobayashi S, Kohno M, Doi M, Tokuhisa T, Okuda S, Suetsugu M, Hisaoka T, Obayashi M, Ohkusa T, Kohno M, Matsuzaki M. FKBP12.6-mediated stabilization of calcium-release channel (ryanodine receptor) as a novel therapeutic strategy against heart failure. *Circulation*. 2003;107:477–484.
12. Wehrens XH, Lehnart SE, Reiken SR, Deng SX, Vest JA, Cervantes D, Coromilas J, Landry DW, Marks AR. Protection from cardiac arrhythmia through ryanodine receptor–stabilizing protein calstabin2. *Science*. 2004;304:292–296.
13. Priori SG, Napolitano C, Tiso N, Memmi M, Vignati G, Bloise R, Sorrentino V, Danieli GA. Mutations in the cardiac ryanodine receptor gene (hRyR2) underlie catecholaminergic polymorphic ventricular tachycardia. *Circulation*. 2001;103:196–200.
14. Laitinen PJ, Brown KM, Piippo K, Swan H, Devaney JM, Brahmbhatt B, Donarum EA, Marino M, Tiso N, Viitasalo M, Toivonen L, Stephan DA, Kontula K. Mutations of the cardiac ryanodine receptor (RyR2) gene in familial polymorphic ventricular tachycardia. *Circulation*. 2001;103:485–490.
15. Tiso N, Stephan DA, Nava A, Bagattin A, Devaney JM, Stanchi F, Larderet G, Brahmbhatt B, Brown K, Bauce B, Muriago M, Basso C, Thiene G, Danieli GA, Rampazzo A. Identification of mutations in the cardiac ryanodine receptor gene in families affected with arrhythmogenic right ventricular cardiomyopathy type 2 (ARVD2). *Hum Mol Genet*. 2001;10:189–194.
16. Yamamoto T, El-Hayek R, Ikemoto N. Postulated role of interdomain interaction within the ryanodine receptor in Ca^{2+} channel regulation. *J Biol Chem*. 2000;275:11618–11625.
17. Yamamoto T, Ikemoto N. Spectroscopic monitoring of local conformational changes during the intramolecular domain-domain interaction of the ryanodine receptor. *Biochemistry*. 2002;41:1492–1501.
18. Yamamoto T, Ikemoto N. Peptide probe study of the critical regulatory domain of the cardiac ryanodine receptor. *Biochem Biophys Res Commun*. 2002;291:1102–1108.
19. Kranias E, Schwarts A, Jungmann RA. Characterization of cyclic 3′:5′-AMP–dependent protein kinase in sarcoplasmic reticulum and cytosol of canine myocardium. *Biochim Biophys Acta*. 1982;709:28–37.
20. Frank K, Tilgmann C, Shannon TR, Bers DM, Kranias EG. Regulatory role of phospholamban in the efficiency of cardiac sarcoplasmic reticulum Ca^{2+} transport. *Biochemistry*. 2000;39:14176–14182.
21. Igarashi-Saito K, Tsutsui H, Yamamoto S, Takahashi M, Kinugawa S, Tagawa H, Usui M, Yamamoto M, Egashira K, Takeshita A. Role of SR Ca-ATPase in contractile dysfunction of myocytes in tachycardia-induced heart failure. *Am J Physiol*. 1998;274:H31–H40.
22. Hajjar RJ, Schmidt U, Kang JX, Matsui T, Rosenzweig A. Adenoviral gene transfer of phospholamban in isolated rat cardiomyocytes: rescue effects by concomitant gene transfer of sarcoplasmic reticulum Ca^{2+})-ATPase. *Circ Res*. 1997;81:145–153.
23. Wehrens XH, Lehnart SE, Huang F, Vest JA, Reiken SR, Mohler PJ, Sun J, Guatimosim S, Song LS, Rosemblit N, D'Armiento JM, Napolitano C, Memmi M, Priori SG, Lederer WJ, Marks AR. FKBP12.6 deficiency and defective calcium release channel (ryanodine receptor) function linked to exercise-induced sudden cardiac death. *Cell*. 2003;113:829–840.
24. Reiken S, Gaburjakova M, Guatimosim S, Gomez AM, D'Armiento J, Burkhoff D, Wang J, Vassort G, Lederer WJ, Marks AR. Protein kinase A phosphorylation of the cardiac calcium release channel (ryanodine receptor) in normal and failing hearts: role of phosphatases and response to isoproterenol. *J Biol Chem*. 2003;278:444–453.
25. Li Y, Kranias EG, Mignery GA, Bers DM. Protein kinase A phosphorylation of the ryanodine receptor does not affect calcium sparks in mouse ventricular myocytes. *Circ Res*. 2002;90:309–316.
26. Ginsburg KS, Bers DM. Modulation of excitation-contraction coupling by isoproterenol in cardiomyocytes with controlled SR Ca^{2+} load and Ca^{2+} current trigger. *J Physiol*. 2004;556:463–480.

Correction

In the article, "Defective Regulation of Interdomain Interactions Within the Ryanodine Receptor Plays a Key Role in the Pathogenesis of Heart Failure," by Oda et al, which appeared in the June 28, 2005, issue of the journal (*Circulation*. 2005;111:3400–3410), the authors would like to note the following error:

In the legend to Figure 3, anti-N-terminal antibody (rabbit serum) was raised against peptide "6EGEDEIQFLRTDDE19," not "24CTATIHKEQQKL35."

The authors regret this error.

DOI: 10.1161/CIRCULATIONAHA.105.170773

(*Circulation*. 2005;112:e291.)

Circulation is available at http://www.circulationaha.org

Journal of the American College of Cardiology
© 2005 by the American College of Cardiology Foundation
Published by Elsevier Inc.

Vol. 46, No. 8, 2005
ISSN 0735-1097/05/$30.00
doi:10.1016/j.jacc.2005.06.069

Longitudinal Structural Determinants of Atherosclerotic Plaque Vulnerability

A Computational Analysis of Stress Distribution Using Vessel Models and Three-Dimensional Intravascular Ultrasound Imaging

Koji Imoto, MD,* Takafumi Hiro, MD, PHD,* Takashi Fujii, MD, PHD,* Akihiro Murashige, MD, PHD,* Yusaku Fukumoto, MD,* Genta Hashimoto, MD,* Takayuki Okamura, MD, PHD,* Jutaro Yamada, MD, PHD,* Koji Mori, PHD,† Masunori Matsuzaki, MD, PHD, FACC*

Ube, Japan

OBJECTIVES This study theoretically examined the longitudinal structural determinants of plaque vulnerability using a color-coded stress mapping technique for several hypothetical vessel models as well as three-dimensional intravascular ultrasound (IVUS) images with use of a finite element analysis.

BACKGROUND It has been shown that an excessive concentration of stress is related to atherosclerotic plaque rupture. However, the local determinants of in-plaque longitudinal stress distribution along the coronary arterial wall remain unclear.

METHODS Using a finite element analysis, we performed a color mapping of equivalent stress distribution within plaques for three-dimensional vessel models as well as longitudinal IVUS plaque images (n = 15). Then, the effects of plaque size, shape, expansive remodeling, calcification, and lipid core on the equivalent stress distribution were examined.

RESULTS The color mapping of vessel models revealed a concentration of equivalent stress at the top of the hills and the shoulders of homogeneous fibrous plaques. Expansive remodeling and the lipid core augmented the surface equivalent stress, whereas luminal stenosis and superficial calcification attenuated the equivalent stress. The location of excessive stress concentration was modified by the distribution of the lipid core and calcification. The thickness of the fibrous cap was inversely related to the equivalent stress within the fibrous cap. However, the color mapping of IVUS plaque images showed that the equivalent stress value at the fibrous cap varied with changes in plaque shape and superficial calcification, even when the thickness of the fibrous cap remained constant.

CONCLUSIONS A distribution analysis of longitudinal stress revealed specific effects of plaque shape, size, and remodeling, as well as effects of the interior distribution of tissue components, on the concentration of stress at the plaque surface. Moreover, fibrous caps of the same thickness did not consistently represent the same vulnerability to rupture. (J Am Coll Cardiol 2005;46: 1507–15) © 2005 by the American College of Cardiology Foundation

Plaque rupture is a major cause of acute coronary syndrome (1,2). It has been shown that plaque rupture frequently occurs in a noncalcified eccentric atherosclerotic plaque with nonsevere stenosis (3–8), expansive remodeling (9–12), a thin fibrous cap (4,13–17), a large lipid core (4,13–16,18–21), and macrophage infiltration (17,22). Therefore, it is thought that a particular cluster of plaque, referred to as vulnerable plaques, is likely to exist, and the development of a modality for detecting this potentially vulnerable portion in the coronary arterial wall is greatly needed in the clinical setting.

In the process of plaque rupture, an excessive concentration of stress at a certain portion of the plaque surface is considered an important factor (23). An in vitro study reported by Loree et al. (13) showed that thinning of the fibrous cap over a subintimal lipid pool dramatically increased peak circumferential stress in the cross section, especially at the shoulder region of eccentric plaques. However, the local determinants of the distribution of in-plaque longitudinal stress along the coronary arterial wall remain unclear. Therefore, the purpose of this study was to clarify the determinants of the distribution of longitudinal stress within plaques, using a color mapping technique based on computational structural analysis. This color mapping was derived from several hypothetical vessel models as well as from three-dimensional intravascular ultrasound (IVUS) images. The structural computation was performed by a finite element analysis using established material parameters for vessel tissue components (13,19,23,24).

METHODS

Design of vessel models. Initially, various idealized vessel models were designed to examine the effects of plaque morphology and tissue components on longitudinal stress

From the Departments of *Molecular Cardiovascular Biology and †Applied Medical Engineering Science, Yamaguchi University Graduate School of Medicine, Yamaguchi, Ube, Japan. This study was partly supported by a grant-in-aid for scientific research of the Ministry of Education, Japan (grant No. (C)(2)14570666), Health and Labour Sciences Research Grants: Comprehensive Research on Cardiovascular Diseases from Ministry of Health, Labour, and Welfare of Japan, and Knowledge Cluster Initiative of the Ministry of Education, Japan. The first two authors contributed equally to this work. This study was presented in part at the 77th scientific sessions of the American Heart Association, New Orleans, Louisiana, 2004.

Manuscript received February 6, 2005; revised manuscript received June 10, 2005, accepted June 14, 2005.

JACC Vol. 46, No. 8, 2005
October 18, 2005:1507–15

Abbreviations and Acronyms

E = Young moduli
G = shear modulus
IVUS = intravascular ultrasound
P = Poisson ratios

distribution inside the plaque. As shown in Figure 1, a cylindrical vessel model was used, in which an atherosclerotic plaque was formed by the revolution of the same longitudinal sectional structure, thereby avoiding the influence of cross-sectional geometrical factors. This cylindrical model had an inner radius of 1.7 mm and a vessel wall thickness of 0.5 mm at the reference site. In the computational simulation, various plaque morphologies were hypothesized with various stenosis severities and types of vessel remodeling. It was assumed that the plaque components consisted of collagen fibers, calcifications, homogenous lipid tissue, and smooth muscle cells. The blood pressure was considered to be uniform along the vessel walls. The effect of blood flow was neglected in this study. There were no structural limitations in terms of the degree of outward expansion.

As in previous established studies (13,23), all of the components of the atherosclerotic plaques were considered to be orthotropic materials with linear elastic properties. In this study, arteries and fibers provided similar material properties in the circumferential (θ) direction, as well as in the axial (z) direction, which differed from those in the radial (r) direction. Each parameter for the material properties defined in this study is shown in Table 1. In Table 1, E_r and E_θ are the Young moduli in the radial and circumferential directions, respectively. $G_{r\theta}$ is the shear modulus in the $r\theta$ plane, where G_{ij} is the ratio of the shear stress to the shear strain in the ij plane. $P_{r\theta}$ and $P_{\theta z}$ are the Poisson ratios in the $r\theta$ and θz planes, respectively. All of these values have been accepted as the representative values of the material properties of atherosclerotic lesions (13,23). It was assumed that lipids and calcifications were nearly incompressible because of their isotropic properties (23). The Young modulus of lipids was estimated to be 1/100th of the circumferential modulus of a normal artery. The Young modulus of calcified plaques was estimated as 10 times that of the plaque E_θ (13).

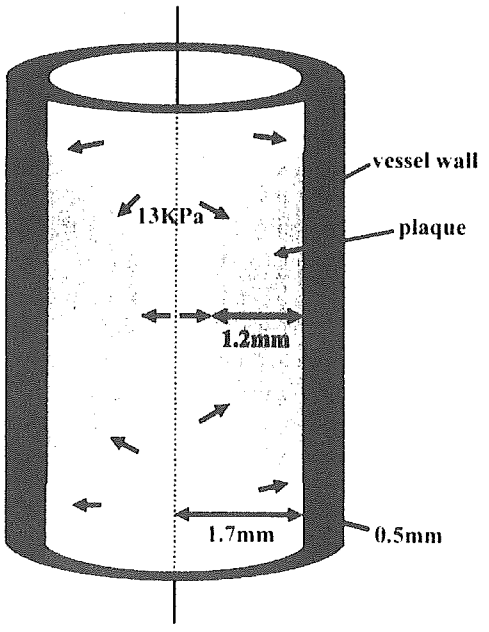

Figure 1. Three-dimensional model. In this vessel model, vessel diameter may vary when a remodeling model is considered.

Structural analysis. The computational structural analysis was performed with a finite element model using a commercially available application (ANSYS 6.0 software, ANSYS Inc., Pittsburgh, Pennsylvania). A complex structure of a vessel model was first divided into smaller subunits designated as elements. The total number of the subunits was approximately 10,000, with a spatial resolution of approximately 100 (10 μm × 10 μm) μm^2. Then, the equivalent stress for each element was calculated. The equivalent stress represented all types of stress for a certain area analyzed, which was calculated from three principal stresses. The structure was automatically meshed with eight-noded quadrilateral plane-strain elements. Each mesh was modified by using an adaptive remeshing algorithm, which was installed in the program. An internal luminal static pressure of 13 kPa (100 mm Hg) was applied along the luminal wall, representing the mean physiological blood pressure in the coronary arteries. Finally, contour plots of equivalent stress were shown on a post-graphics terminal. These contour plots provided two types of colorized mapping, with color codes superimposed on the original structure. One type of mapping was absolute mapping, in which each color code represented a certain range of the absolute value of the equivalent stress; the other type of mapping was relative mapping, in which the color coding was performed by equal division of the range of stress between the maximum and minimum values. According to the computer algorithm, the resulted deformation, such as indentation at the soft part or outward bulging of the normal wall without plaques, was also illustrated.

This study first analyzed the longitudinal stress distribution within plaques for several vessel models with varying structural characteristics of plaque, such as plaque size, plaque shape, stenosis severity, remodeling type, lipid core size, fibrous cap thickness, location and degree of calcification, and so on.

IVUS study. The present study also examined the longitudinal stress distribution in plaques, the structure of which was obtained from the three-dimensional IVUS images. Fifteen human ruptured coronary lesions selected from patients diagnosed with acute coronary syndrome were imaged by IVUS (Atlantis SR pro, 2.8-F, 40-MHz, Boston Scientific Corp./SCIMED, Maple Grove, Minnesota). The transducer was withdrawn automatically using a motorized pullback device (pullback speed, 0.5 mm/s). The IVUS images were all recorded on S-VHS videotape for off-line

Table 1. Material Parameters for Arteries, Plaques, Calcifications, and Lipids Used in Finite Element Models

	Young Moduli (E)			Poisson Ratios (P)			Shear Moduli (G)		
	r	θ	z	rθ	θz	zr	rθ	θz	zr
Artery	10	100	10	0.01	0.27	0.27	50	50	50
Plaque	50	1000	50	0.01	0.27	0.27	500	500	500
Calcification	10,000	10,000	10,000	0.48	0.48	0.48			
Lipid	1	1	1	0.48	0.48	0.48			

r, θ, and z = radial, circumferential, and axial directions, respectively.

analysis. The images were then digitized and analyzed with commercially available software for longitudinal reconstructive IVUS image analysis (Netra IVUS, ScImage Inc., Los Altos, California).

The rupture was defined by an apparent morphology in IVUS images along with comparable clinical history, electrocardiograms, and echocardiograms. No definitive thrombus was detected around the plaque both in IVUS and in angiography. Ruptured plaques with a distinct cavity as well as a significant residual fibrous flap were selected to predict surface morphology before rupture by extrapolating the line of lumen-intima interface.

It was assumed that the ulceration cavity detected by IVUS used to be a lipid core, and that a fibrous cap of a certain thickness used to cover the lipid core. In this in vivo analysis, it was also presumed that the arteries and the plaque components had orthotropic linearly elastic material properties, and that the plaques consisted of homogeneous

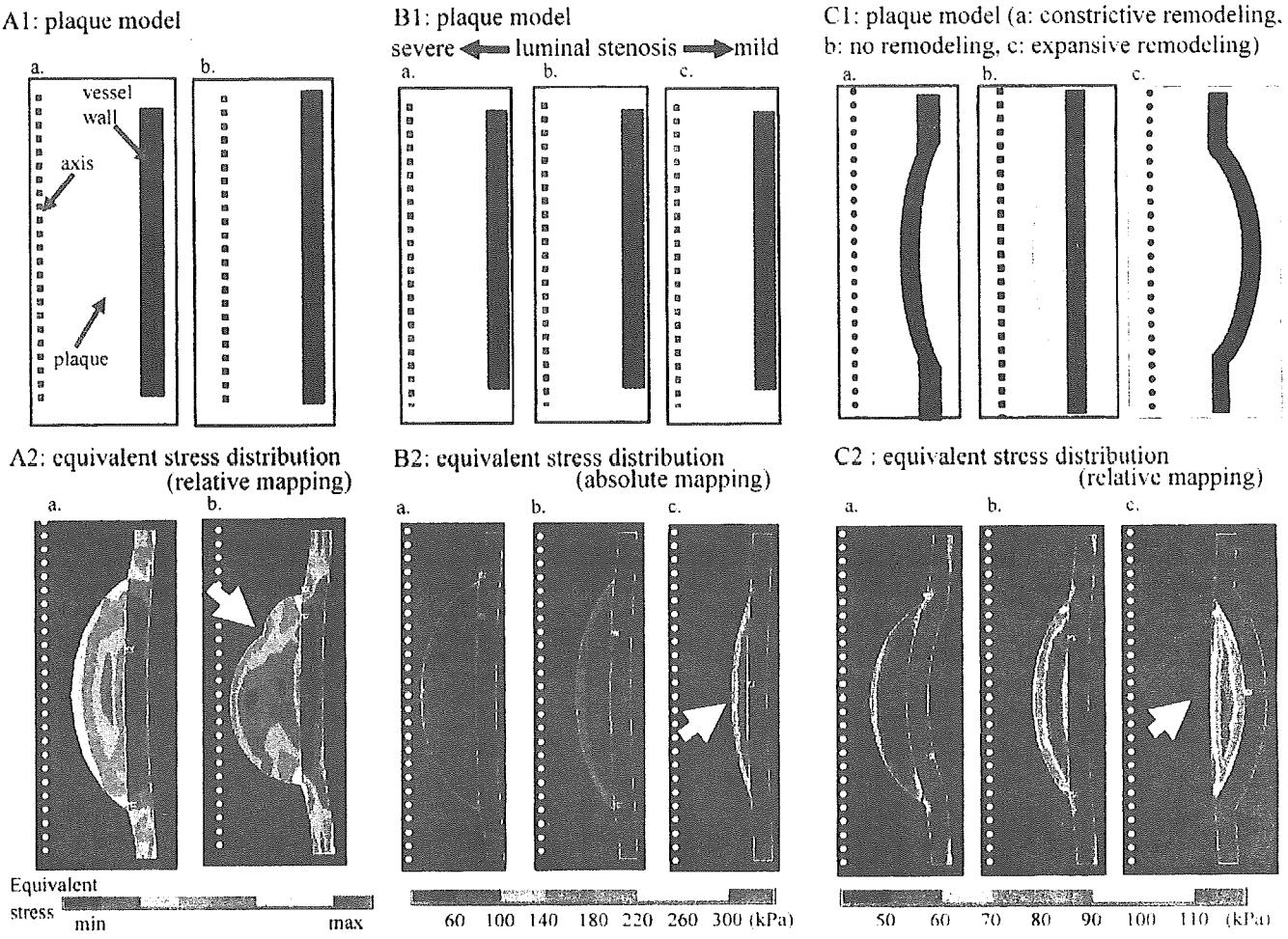

Figure 2. Relationship between stress distribution and plaque shape, luminal stenosis, or vessel remodeling. **(A1, A2)** Color mapping of longitudinal stress distribution within a homogeneous hill-like fibrous plaque model and a complex-shaped model. Relative mapping **(A2)** was performed in the automatically determined window between the maximum and minimum value of stress. The **arrows** designate the sites of stress concentration. **(B1, B2)** Relationship between luminal stenosis and stress distribution. Absolute mapping **(B2)** represents the distribution of the absolute value of equivalent stress. There was a negative relationship between the equivalent stress and luminal stenosis. **(C1, C2)** Relationship between vessel remodeling and stress distribution. The equivalent stress at the plaque surface of arteries with expansive remodeling was greater than that of arteries with constrictive remodeling, when the plaque thickness remained constant.

JACC Vol. 46, No. 8, 2005
October 18, 2005:1507–15

fibrous tissue, with the exception of the ulcerous cavities and calcifications. However, the original thickness of the fibrous cap of ruptured plaques was unknown. Therefore, in this study, fibrous caps with various thicknesses were considered for the same plaque. Previous in vitro study (19) of human atherosclerotic materials has shown that fibrous caps usually fracture when the static stress exceeds 300 kPa. Therefore, the critical value for fibrous cap thickness, under which the stress on the fibrous cap would exceed 300 kPa, was also calculated for each plaque. This critical thickness was obtained with the abovementioned computer simulation of finite element models. When the critical fibrous cap is thin, it means that the plaque therefore seemed to be less vulnerable. The data were then used to conduct a computational stress analysis using the finite element model for the purpose of color mapping the longitudinal stress distribution, which was superimposed onto the original IVUS images.

This study was approved by the Institutional Review Board of the Hospital of Yamaguchi University School of Medicine. All patients provided signed informed consent to participate in the study before IVUS was performed.

RESULTS

Study of vessel models. This study showed the longitudinal stress distribution within plaques using a color-coded representation. Figure 2A illustrates the longitudinal distribution of equivalent stress within a hill-like homogeneous plaque model by use of relative color mapping. The concentration of equivalent stress could be observed at the top of the plaque hills, as well as at its shoulders. When there was a distortion of plaque shape, the stress was concentrated not only at the summits and shoulders, but also at dips in the irregular surfaces of plaque hills. There was a negative relationship between equivalent stress and luminal stenosis (Fig. 2B). When there was a remodeling of the vascular diameter at a constant maximum plaque thickness, the equivalent stress at the plaque surface of arteries with expansive remodeling was greater than that of arteries with constrictive remodeling (Fig. 2C).

When there was a lipid core, the stress was particularly concentrated at a localized surface area just above the lipid core (Fig. 3). The size of the lipid core had no influence on the surface stress value, given that the thickness of the fibrous cap

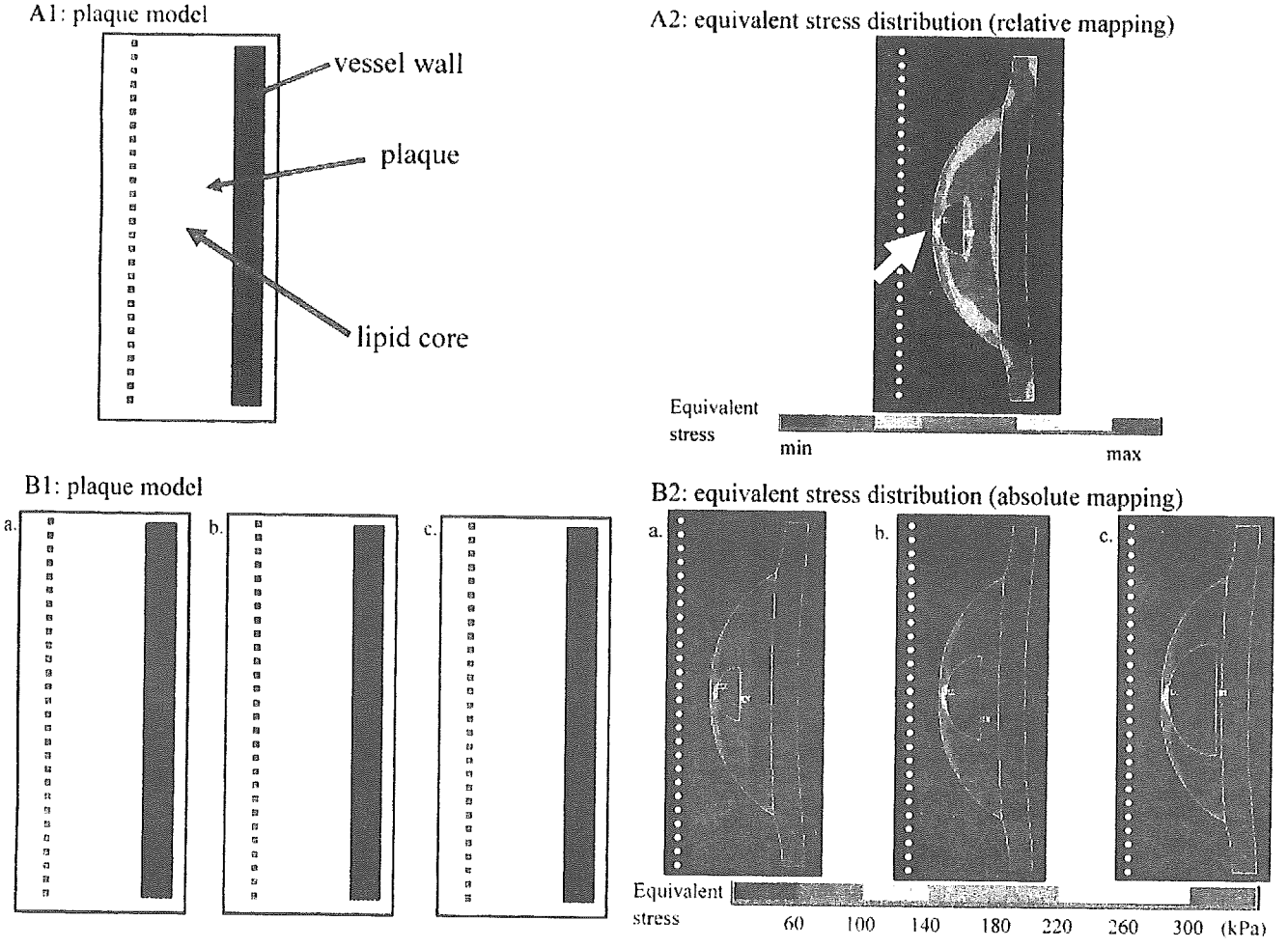

Figure 3. Effect of lipid core on stress distribution. The **arrow** indicates the point of stress concentration at a localized surface area just above the lipid core **(A2)**. The size of the lipid core did not influence the value of the surface stress **(B2)**, provided the fibrous cap thickness remained constant. **(A1, B1)** Plaque models used. **(A2, B2)** Mapping of stress distribution of the corresponded model.

remained constant. However, the thickness of the fibrous cap exerted a great impact on the surface equivalent stress of the plaque, namely, the thinner the fibrous cap, the greater the surface equivalent stress, given that the size of the lipid core remained constant (Fig. 4). In this idealized model, the peak equivalent stress reached beyond the empirical critical level leading to plaque rupture, when the fibrous cap was thinner than 80 μm. Superficial calcifications led to a decrease in surface stress, whereas calcification at the bottom of the plaque exerted no influence on the surface equivalent stress value. As in Figure 5, a superficial calcification adjacent to the lipid core attenuated the peak stress value at the plaque surface just above the lipid core. There was an inverse relationship between the surface equivalent stress and the thickness of the fibrous cap. The stress value increased dramatically when the fibrous cap was thinner than 80 μm. However, when there was a surface calcification near the lipid core, the surface equivalent stress was smaller with the same fibrous cap thickness, such that the inverse relationship shifted leftward and downward (Fig. 6).

IVUS study. Figure 7 shows representative examples of the color mapping of longitudinal stress distribution using longitudinal IVUS images. In case 1, the critical thickness of the fibrous cap leading to rupture was 50 μm, whereas this value was 10 μm in case 2. In case 2, there was a superficial calcification close to the rupture point. Table 2 shows the profile of the 15 ruptured plaques analyzed. The IVUS study showed that the critical thickness of fibrous caps leading to rupture varied between <10 μm and 200 μm.

DISCUSSION

This study was the first showing the longitudinal structural determinants of plaque vulnerability by use of a simplified computational analysis of stress distribution within atherosclerotic plaques using vessel models and three-dimensional intravascular ultrasound imaging. Furthermore, this study also showed that the critical thickness of fibrous caps leading to rupture varied substantially with differences in plaque structure, especially with differences in the degree of calcification.

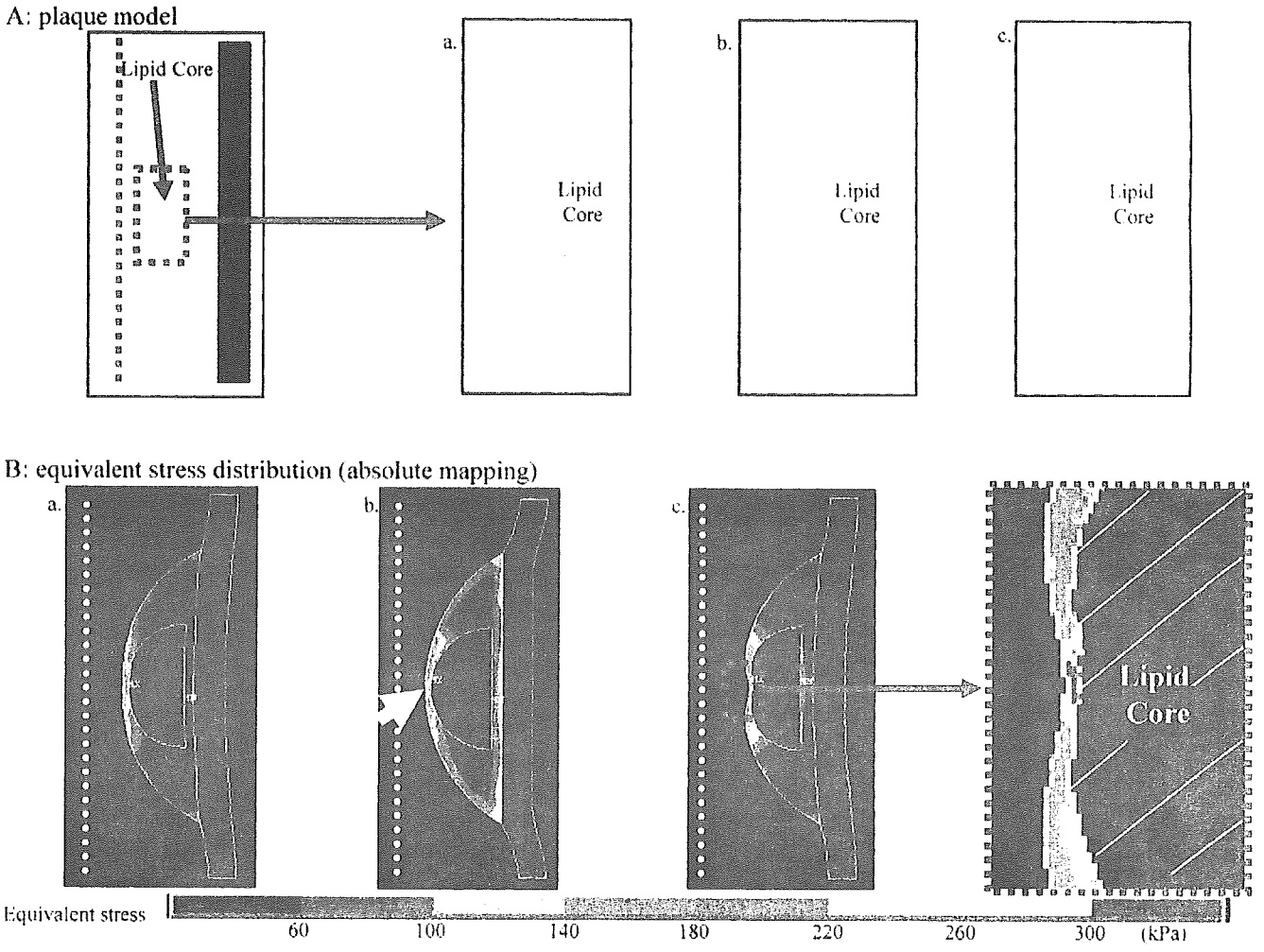

Figure 4. Effect of fibrous cap thickness (a, 90 μm; b, 80 μm; c, 40 μm) on stress distribution. When the fibrous cap was thinner than 80 μm, the stress was markedly elevated (arrow). (Aa, Ab, Ac) Plaque models used. (Ba, Bb, Bc) Mapping of stress distribution of the corresponded model.

JACC Vol. 46, No. 8, 2005
October 18, 2005:1507–15

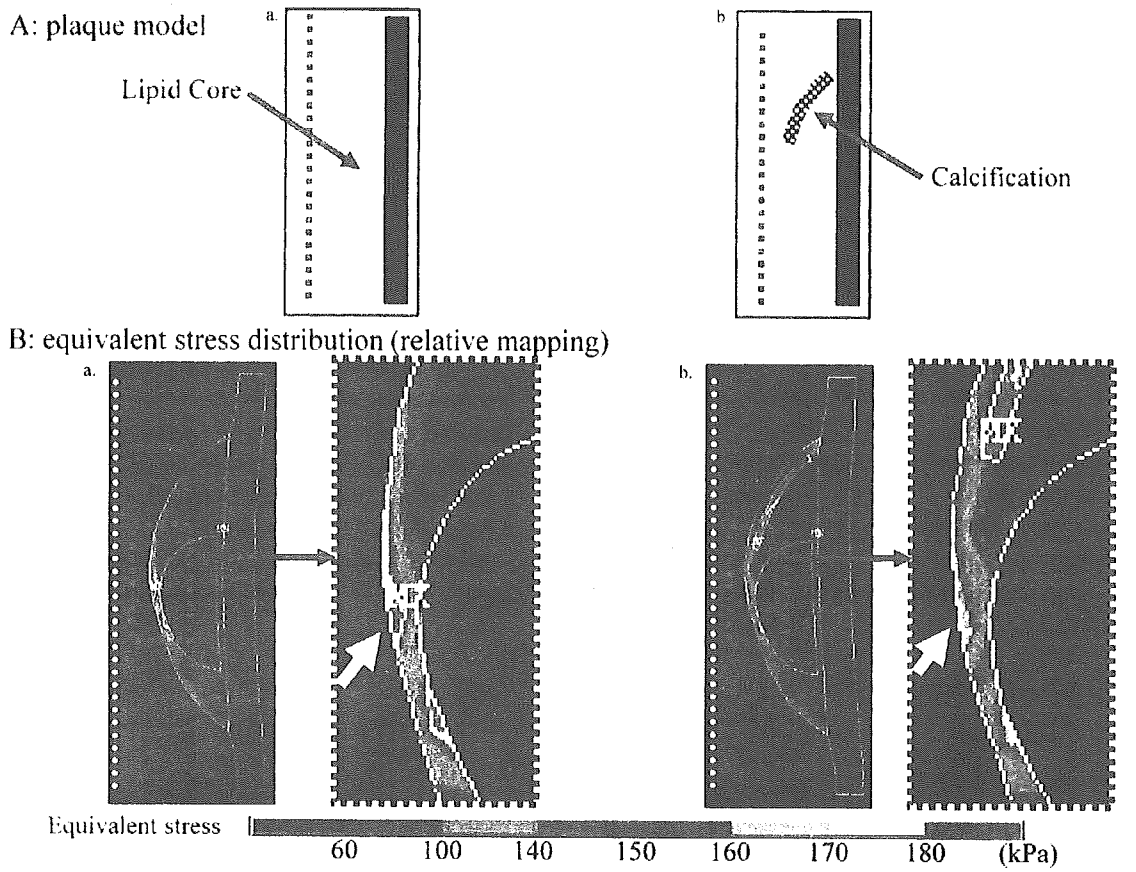

Figure 5. The effect of surface calcifications on the distribution of stress in the surrounding tissue. The size and the place of the lipid core remained constant. A superficial calcification adjacent to the lipid core attenuated the peak stress value at the plaque surface just above the lipid core **(arrow)**. **(Aa, Ab)** Plaque models used. **(Ba, Bb)** Mapping of stress distribution of the corresponded model.

Plaque size, shape, vessel remodeling, and plaque stress. Previous cross-sectional structural analyses of plaque stress distribution have shown that the shoulder regions of eccentric plaques are likely to exhibit stress concentration, leading to a susceptibility to rupture (13). However, the results of this study indicated that longitudinal plaque shape is also important for predicting the location of stress concentration within plaques.

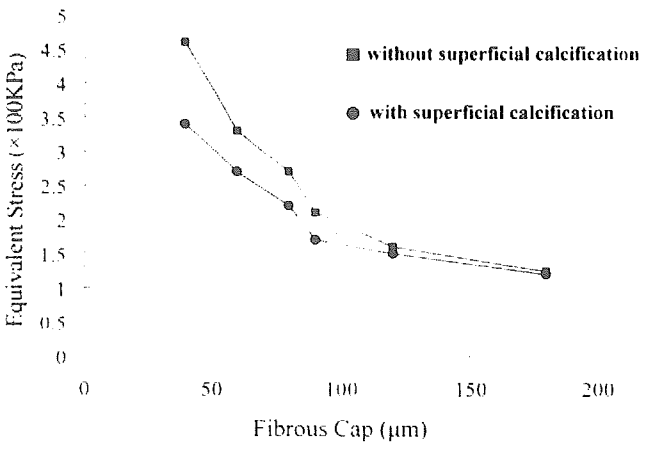

Figure 6. Effect of superficial calcifications on the relationship between the fibrous cap thickness and the peak equivalent stress at the plaque surface. The equivalent stress increased dramatically when the fibrous cap thickness became <80 μm. This increase shifted leftward and downward when there was a superficial calcification close to the area of interest.

Our study showed that increasing either plaque volume or the severity of stenosis decreased the degree of stress concentration. These findings were compatible with those of a previous cross-sectional structural analysis of plaques (13). According to the LaPlace law, the tensile stress on the wall of a luminal structure is correlated with luminal pressure and diameter, and is inversely related to the thickness of the wall. Increasing plaque volume thus increases the thickness of a wall and decreases the luminal diameter (unless there is vessel remodeling), thereby leading to a decrease in the surface stress of the plaque. The present results may therefore account for previous serial angiographic analyses showing that the culprit lesion before the acute event frequently had <50% diameter stenosis (3–8). Based on recent IVUS studies, it is likely that plaque regression or less progression that may not lead to stress attenuation is associated with a decrease in the risk of future cardiac events (9–11). Therefore, this paradoxical consequence could be attributed to simultaneous changes in plaque composition and fibrous cap thickness.

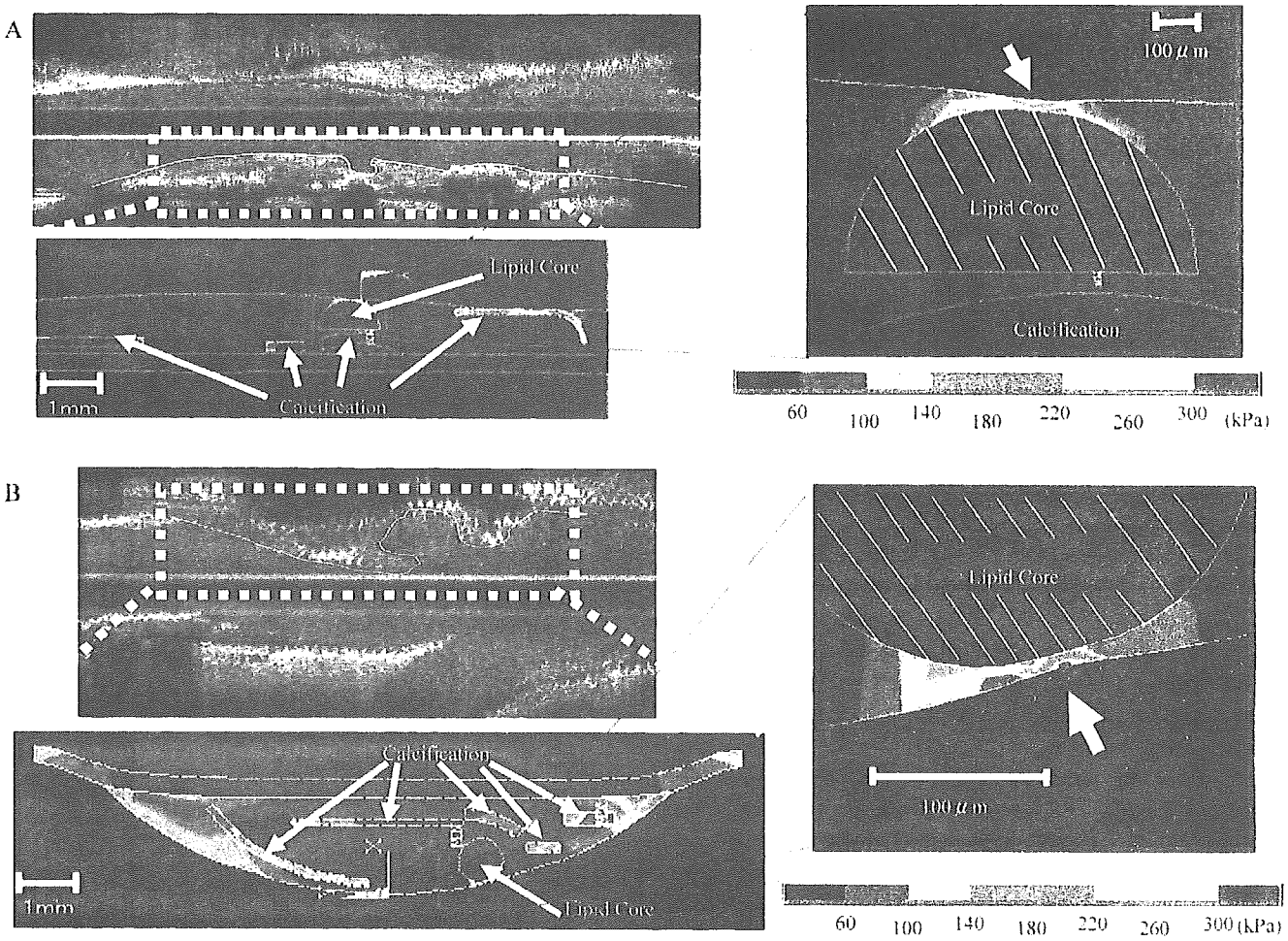

Figure 7. Representative examples of the three-dimensional IVUS images and the color mappings of longitudinal stress distribution. The arrows show rupture points. In case 1, the critical thickness of the fibrous cap in terms of rupture was 50 μm **(A)**. However, the thickness in case 2 had to be reduced to <10 μm to reach the critical point in terms of plaque rupture **(B)**. Thus, case 2 seemed to represent a less vulnerable plaque than case 1, although the fibrous cap thickness was the same. **(A)** Case 1; **(B)** case 2.

Table 2. Ruptured Plaque Characteristics Detected by IVUS and Its Simulated Critical Fibrous Cap Thickness

Case	Coronary Artery	Longitudinal Plaque Length	Plaque Thickness	Vessel Diameter	Ulcer Diameter	Superficial Ca	D (mm)	Deep Ca	Critical Fibrous Cap Thickness (μm)
1	LAD	14.6	2.6	5.2	3.1	+	0.8	+	<1
2	RCA	21.0	1.9	4.1	3.2	+	0	+	40
3	LAD	40.0	1.7	4.6	1.8	+	2.4	+	50
4	LAD	12.3	1.2	4.9	2.1	–	–	–	200
5	RCA	26.4	2.0	4.1	0.8	–	–	+	<10
6	LAD	13.2	2.1	5.1	1.7	+	0.7	+	20
7	LAD	5.9	1.2	4.0	0.9	+	2.0	+	15
8	LAD	5.3	1.4	3.6	0.7	–	–	+	60
9	LAD	5.1	1.3	3.3	0.8	–	–	+	60
10	LAD	15.5	2.6	4.0	1.5	–	–	+	<10
11	LAD	12.0	2.1	3.9	1.0	–	–	–	<10
12	LAD	8.2	2.1	3.5	1.8	–	–	+	<10
13	LAD	10.6	1.3	2.9	1.7	–	–	–	20
14	LAD	11.0	1.5	5.2	1.2	+	1.2	+	140
15	LAD	11.3	1.7	3.3	0.6	–	–	+	<10

Ca = calcification; D = distance between edge of superficial calcification and orifice of ulceration; IVUS = intravascular ultrasound; LAD = left anterior descending artery; RCA = right coronary artery.